Cell

Functional and antigenic landscape of the Nipah virus receptor-binding protein

Graphical abstract

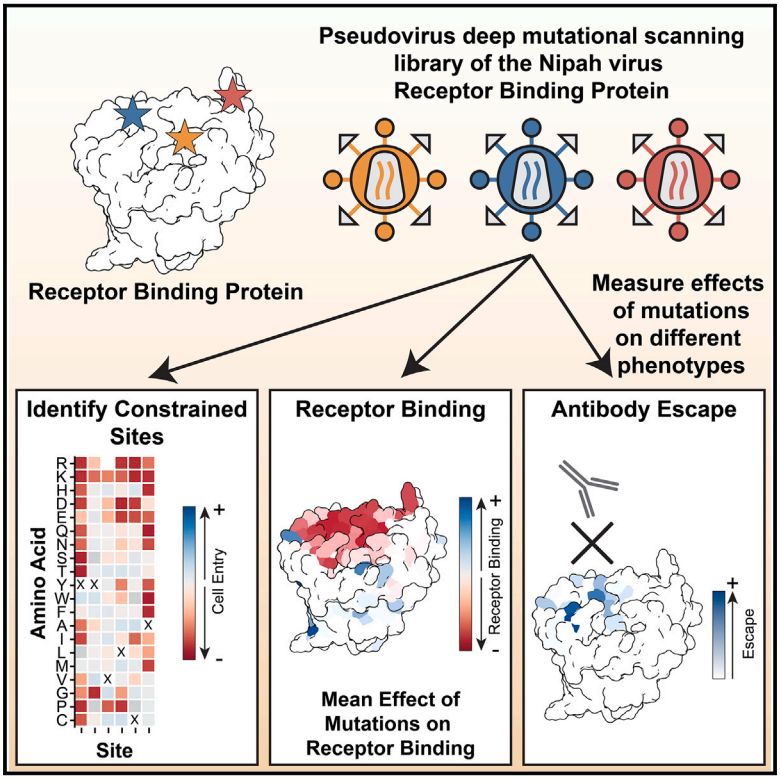

Authors

Brendan B. Larsen, Teagan McMahon, Jack T. Brown, ..., James E. Crowe, Jr., David Veesler, Jesse D. Bloom

Correspondence

jbloom@fredhutch.org

In brief

Nipah virus is a zoonotic virus that spills over to humans and causes infections with a high mortality rate. Deep mutational scanning of the Nipah virus receptor-binding protein provides insights into viral receptor binding and entry into cells as well as antibody escape, thus providing an understanding of viral evolution as well as a roadmap for the design of therapeutics.

Highlights

- Performed deep mutational scanning of the Nipah virus receptor-binding protein
- Used a pseudovirus platform to measure mutation effects safely
- Measured how all mutations affect cell entry, receptor binding, and antibody escape
- Identified and validated mutations that alter receptor affinity

Larsen et al., 2025, Cell *188*, 2480–2494
May 1, 2025
https://doi.org/10.1016/j.cell.2025.02.030

CellPress

CellPress
OPEN ACCESS

Cell

Article

Functional and antigenic landscape of the Nipah virus receptor-binding protein

Brendan B. Larsen,[1] Teagan McMahon,[1] Jack T. Brown,[2] Zhaoqian Wang,[2] Caelan E. Radford,[1] James E. Crowe, Jr.,[3] David Veesler,[2,4] and Jesse D. Bloom[1,4,5,*]

[1]Basic Sciences Division and Computational Biology Program, Fred Hutchinson Cancer Center, Seattle, WA 98109, USA
[2]Department of Biochemistry, University of Washington, Seattle, WA 98195, USA
[3]Department of Pathology Microbiology and Immunology, The Vanderbilt Vaccine Center, and Department of Pediatrics, Vanderbilt University Medical Center, Nashville, TN 37232, USA
[4]Howard Hughes Medical Institute, Seattle, WA 98195, USA
[5]Lead contact
*Correspondence: jbloom@fredhutch.org
https://doi.org/10.1016/j.cell.2025.02.030

SUMMARY

Nipah virus recurrently spills over to humans, causing fatal infections. The viral receptor-binding protein (RBP or G) attaches to host receptors and is a major target of neutralizing antibodies. Here, we use deep mutational scanning to measure how all amino-acid mutations to the RBP affect cell entry, receptor binding, and escape from neutralizing antibodies. We identify functionally constrained regions of the RBP, including sites involved in oligomerization, along with mutations that differentially modulate RBP binding to its two ephrin receptors. We map escape mutations for six anti-RBP antibodies and find that few antigenic mutations are present in natural Nipah strains. Our findings offer insights into the potential for functional and antigenic evolution of the RBP that can inform the development of antibody therapies and vaccines.

INTRODUCTION

Nipah virus is a zoonotic negative-sense RNA virus that circulates in *Pteropus* bats across Southeast Asia.[1–4] Nipah virus and some other viruses in the *Henipavirus* genus spill over into humans and livestock with fatality rates approaching 70%.[5–7] Nipah virus was first identified during an outbreak in Malaysia in 1998 with subsequent (almost annual) spillovers in Bangladesh and India. These spillovers have sometimes resulted in human-to-human transmission, raising concerns about the potential for a larger outbreak.[8,9] No vaccines or specific therapeutics are approved for use in humans against Nipah virus.

Nipah virus has two different surface proteins that mediate cell entry: the tetrameric receptor-binding protein (RBP or G) and the trimeric fusion (F) protein. RBP binds to the cell-surface proteins ephrin-B2 or -B3 (EFNB2/3), either of which can function as the viral receptor.[10–13] EFNB2 and EFNB3 are members of a protein family that is crucial for vertebrate development and cell signaling and are highly conserved among mammals,[14–16] concurring with the unusually wide Nipah virus species tropism. The Nipah virus RBP binds both EFNB2 and EFNB3 despite these two receptor proteins only sharing 40% amino-acid identity.[12] The affinity of RBP for EFNB2 is among the highest of any known viral protein for its receptor, while the affinity for EFNB3 is substantially lower.[13] Following binding to its receptor(s), the RBP undergoes a conformational shift that triggers F to fuse the viral and cell membranes and initiate infection.[17]

Potent RBP-directed monoclonal antibodies have been identified that neutralize Nipah virus and prevent disease in animal models.[18–21] Antibodies and vaccines are currently being developed as a defense against Nipah virus,[22–29] but for some other viruses, evolution has rendered such countermeasures less effective.[30] *In vitro* studies have identified some RBP antibody-escape mutations,[31,32] but such studies have been limited due to the inherent difficulty of working with Nipah virus itself, which is a biosafety level 4 (BSL-4) select pathogen. There are also relatively few sequences available of natural Nipah virus isolates, limiting the inferences that can be made about evolutionary constraints from sequence variation.

Here, we experimentally measure the effects of all amino-acid mutations to the RBP ectodomain using a BSL-2 lentiviral pseudovirus deep mutational scanning (DMS) platform.[33,34] By coupling experimental selections on variant libraries with deep sequencing, we quantify how mutations affect three RBP phenotypes: cell entry, receptor binding, and antibody escape. Collectively, these results elucidate the evolutionary potential of a key protein from this pathogenic zoonotic virus with pandemic potential.

RESULTS

A pseudovirus DMS library of the Nipah virus RBP

To measure how mutations to RBP impact cell entry, receptor binding, and antibody evasion, we utilized a recently

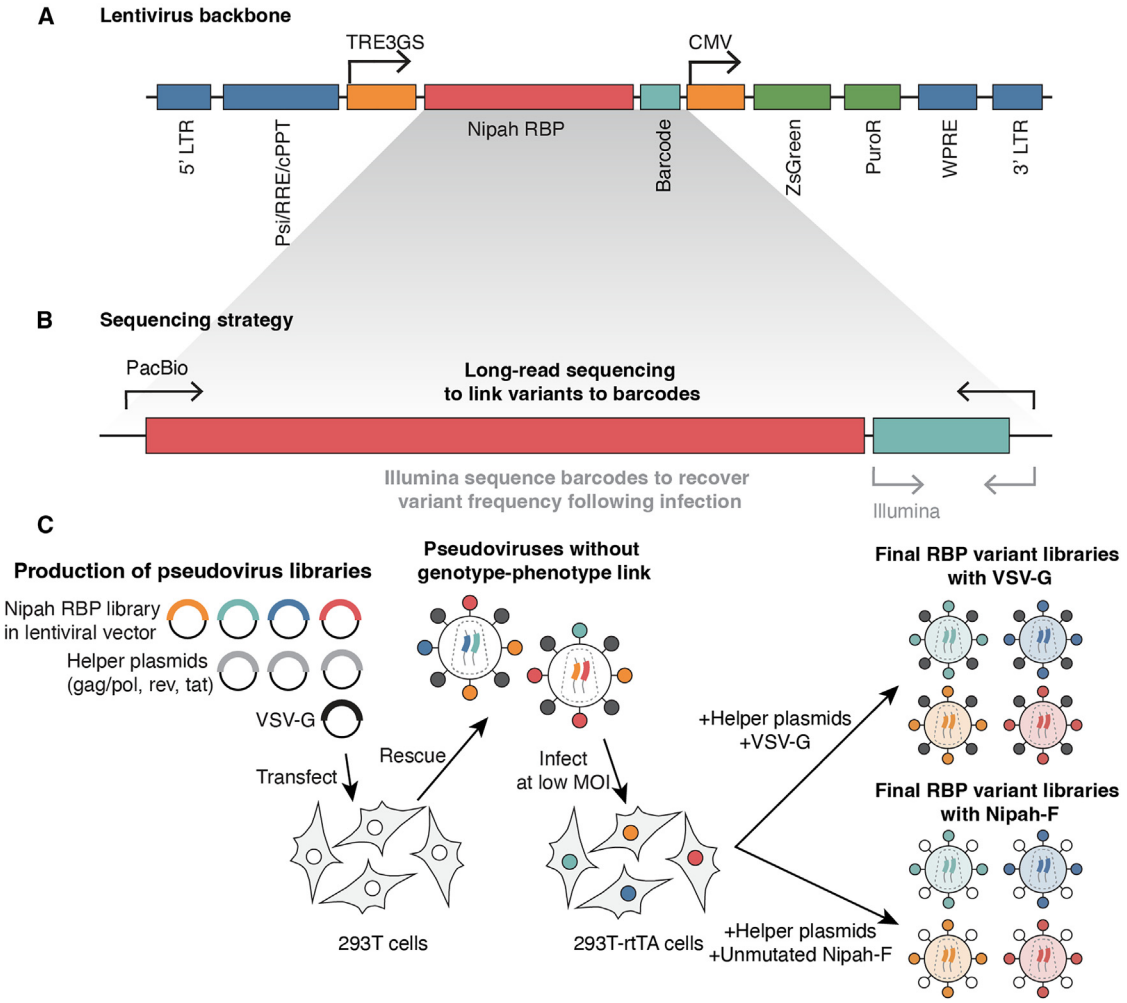

Figure 1. Deep mutational scanning workflow

(A) Lentiviral backbone. Mutagenized RBP variants followed by unique 16-nucleotide barcodes were cloned into a lentiviral vector downstream of an inducible TRE3GS promoter. ZsGreen and puromycin resistance genes (PuroR) are downstream of a CMV promoter. The vector also contains essential lentiviral motifs, including the 5′ and full-length 3′ long-terminal repeats (LTRs), the psi packaging element (Psi), rev response element (RRE), and central polypurine tract (cPPT). The Woodchuck hepatitis virus post-transcriptional regulatory element (WPRE) is included for increased transgene expression.

(B) Sequencing of RBP variants and barcodes. To link variants in RBP with specific barcodes, we PCR-amplified a region that spans the whole RBP gene and barcode region and then used long-read PacBio sequencing to determine which RBP mutant was linked to each barcode. For DMS experiments, we could then simply PCR amplify and Illumina sequence the short barcode region to identify the full RBP sequence.

(C) Strategy to make genotype-phenotype-linked pseudoviruses. A barcoded library of codon-optimized RBP variants based on the Nipah Malaysia strain was cloned into an HIV-based lentiviral vector (shown in A) and transfected into 293T cells with additional lentiviral helper plasmids (encoding gag/pol, rev, tat) and a plasmid encoding the envelope protein from the vesicular stomatitis virus (VSV-G), which has broad tropism. Pseudoviruses rescued from transfections are not suitable for DMS as they lack a genotype-phenotype link, since each pseudodiploid virion contains two genomes and different RBP variants on the surface. To establish a link between the RBPs on the virion surface and the genotype, we infected 293T-reverse tetracycline-controlled transactivator (rtTA) cells at a low multiplicity of infection (MOI < 0.01) to ensure a single integration per cell. Cells containing an integrated provirus are selected with puromycin, creating a cell-stored library of RBP mutants in a lentiviral backbone. Re-transfection of helper plasmids into cell-stored libraries plus either VSV-G or unmutated Nipah F generates virions that have a single RBP protein variant on their surface and encode an identifying barcode in their genome.

See also Figure S1.

developed DMS platform[33,34] to create genotype-phenotype-linked libraries of lentiviruses pseudotyped with mutants of RBP alongside the unmutated Nipah F protein (Figure 1). The pseudotyped lentiviruses are non-replicative and encode no viral proteins other than the RBP, and so provide a tool to safely study RBP mutants at BSL-2. We mutagenized RBP from the Nipah Malaysia strain, which was the first described isolate of this virus and is widely used in other published work (Figure 2A). The Nipah Malaysia RBP differs from other known Nipah RBPs by a maximum of 29 amino-acid mutations. We truncated 32 and 22 amino acids from the cytoplasmic tails of RBP and F, respectively, which increased pseudovirus

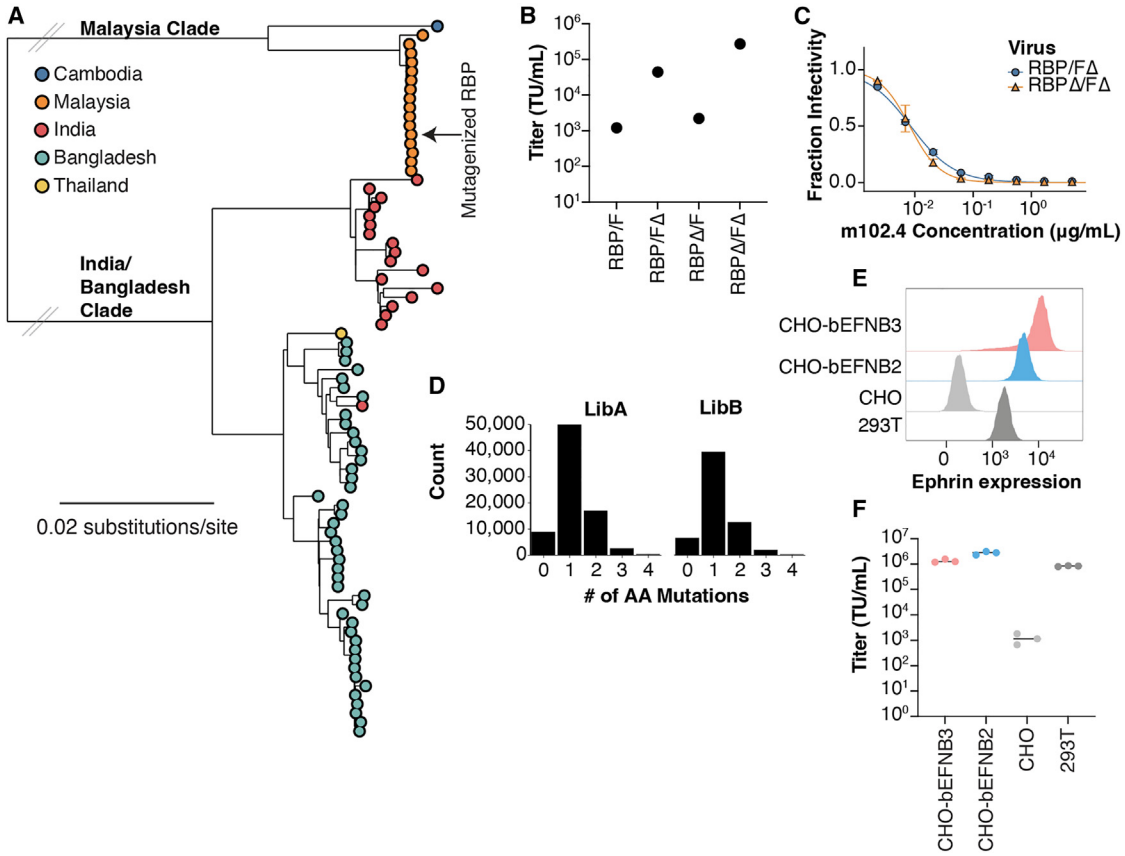

Figure 2. Modifications to the Nipah virus RBP for efficient pseudotyping

(A) Nipah virus evolution and source of parental sequence used for DMS. A maximum likelihood phylogeny was inferred from all publicly available full-length Nipah virus nucleotide sequences downloaded from GenBank (on Jan-3-2024). The tree was inferred with IQ-Tree v2.2.2.6 using a TIM2 substitution model. Scale bar shows the number of nucleotide substitutions per site. Tips are colored by country of origin. The Malaysia strain used in our DMS study is indicated with an arrow and text. The two long internal branches were truncated to reduce empty space and indicated with double slash marks ("//").

(B and C) Truncating the cytoplasmic tails of the Nipah virus RBP and F proteins improves titers of pseudotyped lentiviral particles without affecting antigenicity. Based on prior research on pseudotyping lentiviruses with Nipah RBP/F, we removed 32 and 22 amino acids from the cytoplasmic tails of RBP and F proteins, respectively. This modification improved pseudovirus titers, so we utilized the glycoproteins with truncated cytoplasmic tail in all subsequent experiments.

(B) Titers of unmutated Nipah RBP/F pseudoviruses titered in HEK293T cells with or without cytoplasmic tail truncations (indicated by Δ) in RBP and/or F.

(C) Neutralization by the anti-RBP monoclonal antibody m102.4 of pseudovirus with full-length RBP compared with RBP with a cytoplasmic tail truncation. The neutralization curves are indistinguishable, suggesting the cytoplasmic tail deletion does not affect antigenicity.

(D) Statistics of RBP mutant library composition. Histogram showing the distribution of amino-acid mutations per variant for each library.

(E and F) *Pteropus alecto* EFNB2/3 expression levels and susceptibility to infection by unmutated RBP/F-pseudotyped lentiviruses of the stable clones used as target cells in this study. CHO cells were transduced with a lentiviral vector expressing bat (*Pteropus alecto*) EFNB2 (bEFNB2) or EFNB3 (bEFNB3) downstream of an EF1-alpha promoter, and sorted individual cells were expanded. Clones were selected to have low bEFNB2/bEFNB3 expression (to more closely approximate expression in 293T cells) (E) flow cytometry staining data using EphB3-Fc to determine relative expression of ephrin. EphB3 is a natural ligand of all ephrin-B proteins. (F) Titers obtained in different cell lines of lentivirus pseudotyped with unmutated Nipah ΔRBP and ΔF produced by transfection of 293T cells (performed in triplicate).

titers without apparent effect on RBP antigenicity[35,36] (Figures 2B and 2C).

We made duplicate mutant libraries targeting all amino-acid mutations of the RBP ectodomain (residues 71 to 602), for a total of 532 × 19 = 10,108 mutations. Our final duplicate libraries contained 78,450 and 60,623 unique barcoded RBP variants that each covered >99.5% of all possible mutations (Table S1). Most RBP variants carried just a single amino-acid mutation, although there were some variants with multiple mutations (Figure 2D).

We created target cells that expressed only EFNB2 or EFNB3 to distinguish the effects of RBP mutations on usage of each receptor. To do this, we transduced either EFNB2 or EFNB3 into Chinese hamster ovary (CHO) cells, which do not express any ephrins[13] (Figure 2E). We used EFNB2/3 orthologs from a natural Henipavirus host, the black flying fox (*Pteropus alecto*),[37] to avoid the possibility that our experiments could generate potentially hazardous information[38,39] about mutations that adapted RBP to better bind to human receptors. We refer to these bat orthologs as bEFNB2 or bEFNB3. They share 95% and 97% amino-acid identity with the corresponding human proteins. Both bEFNB2- and bEFNB3-expressing CHO cells could be efficiently infected with Nipah RBP pseudovirus (Figure 2F).

Effects of RBP mutations on cell entry

We measured the effects of all RBP amino-acid mutations on pseudovirus entry in CHO-bEFNB2 and CHO-bEFNB3 cells by quantifying the ability of each barcoded pseudovirus variant to enter cells when pseudotyped with its RBP mutant and unmutated F versus vesicular stomatitis virus G protein (VSV-G) (Figure S1A). Because our libraries contain some RBPs encoding multiple mutations (Figure 2D), we deconvolved the effects of individual mutations using a global epistasis model. These deconvolved effects were highly correlated with the effects measured for single-mutant variants only (Figure S2A).[40] After excluding low-confidence measurements, our dataset contained cell-entry measurements for 97% and 96% of the 10,108 possible single amino-acid mutants of the RBP ectodomain in CHO-bEFNB2 and CHO-bEFNB3 cells, respectively. Measurements of mutational effects on cell entry made using the two independent libraries were highly correlated (Figure S2B), and throughout this paper, we report the average measurement across the two libraries.

Mutations had varied effects on RBP-mediated entry in CHO-bEFNB3 cells, ranging from highly deleterious to well tolerated (Figure 3; see also link to CHO-bEFNB2 data in STAR Methods). Prior cryoelectron microscopy structures of the Nipah virus RBP ectodomain tetramer show that it consists of four major regions designated stalk, neck, linker, and head[31] (Figures S2C and S2D). Functional constraints were particularly high in the stalk and neck regions, the area of the head interacting with the EFNB2/3 receptors, and the dimerization interface between distal heads (Figures 4A–4D).

The RBP neck was the most functionally constrained region, probably due to its critical role in tetramerization, stability, and F-triggering[41] (Figure 4C). The neck forms a stacked β-sandwich, encircled by glycans linked to N159 (Figure 4E). The cysteines at sites 158 and 162 were intolerant to any mutations, consistent with previous mutagenesis work[41] and their key structural role.[31] The neck is particularly rich in prolines and hydrophobic residues, which were generally functionally constrained (Figures 4E and S2E). Previous work suggested the N-linked glycan at position 159 is important for F-triggering.[42] Our results indicate strong constraint on site 159, as most mutations at this site were highly deleterious, with the exception of mutations to the negatively charged D and E amino acids (Figure 3). However, mutations to non-S/T amino acids at site 161, which disrupt the N-linked glycosylation motif, were also largely tolerated, suggesting the glycan is dispensable for entry (Figure 3).

The distal heads form a complex, asymmetric dimerization interface with multiple interacting residues. Nearly all mutations at sites Y205, T206, P208, R258, G259, and F266 in the dimerization interface drastically reduced cell entry (Figures 3 and 4F). At site Y205, the only non-deleterious change was mutation to a tryptophan, another aromatic side chain (Figure 3), likely due to retention of cation-pi and van der Waals interactions between the residue 205 aromatic side chain and R258 from the adjacent head (Figure 4F). Although several sites in the linker (164–173) from chain B contact chain A residues in the dimer interface (Figure 4F), most mutations at linker sites had minor effects on entry, indicating these individual interactions are non-essential (Figures 3 and 4F).

Most mutations at sites that directly contact the receptor were highly deleterious for entry in CHO-bEFNB3 cells (Figure 4G). Sites on the periphery of the binding pocket were more tolerant to mutations than those within the central binding pocket (Figure 4G). D555, Q388, and R402 each tolerated several mutations, whereas sites N557, E579, and Y581 were the most constrained of all receptor-interface sites, and all mutations were highly deleterious (Figures 4G, S2F, and S2G).

The effects of mutations on entry in CHO-bEFNB2 and CHO-bEFNB3 cells were largely similar (Figure 4H). However, some receptor-contact sites were more tolerant to mutations for entry into CHO-bEFNB2 than CHO-bEFNB3 cells (Figures 4H and S2G). This difference is likely because RBP has a greater than one log higher binding avidity for EFNB2 compared with EFNB3,[13] meaning it can tolerate more reduction in binding while still maintaining efficient entry in bEFNB2-expressing cells, at least in the cell-culture context of our experiments.

To determine whether our measurements of mutational effects on cell entry by the Nipah RBP are consistent with viral evolution in a closely related virus, we identified all mutations in Hendra virus RBPs (which share ∼80% amino-acid sequence identity with Nipah). Nearly all Hendra virus mutations were tolerated for entry in both CHO-bEFNB2 and CHO-bEFNB3 cells in our DMS of the Nipah RBP (Figure S2H). This observation indicates that our measurements on the parental Nipah RBP also reflect much of the purifying selection on closely related Henipaviruses, since if there were large epistatic shifts in the effects of mutations, then we might expect Hendra RBP to contain some mutations that are deleterious for Nipah cell entry.

To validate the DMS measurements of mutational effects on cell entry, we constructed eight pseudoviruses with single RBP mutations spanning a range of entry effects from DMS and evaluated their entry in CHO-bEFNB2 and CHO-bEFNB3 cells relative to unmutated RBP. Cell entry for these individual pseudoviruses strongly correlated with the DMS measurements ($r = 0.89$ for CHO-bEFNB3, Figure 4I; $r = 0.79$ for CHO-bEFNB2, Figure S2I).

Effects of RBP mutations on receptor binding

Mutations to RBP can affect cell entry by many mechanisms, including altering receptor binding, fusion triggering, protein stability, or protein expression. To partially deconvolve these mechanisms, we sought to measure the effects of RBP mutations on binding to bEFNB2 and bEFNB3. Inspired by prior studies that showed that inhibition of viral entry by soluble receptor is proportional to receptor-binding affinity,[43–45] we incubated our RBP pseudovirus libraries with different concentrations of soluble bEFNB2 or bEFNB3 to measure how RBP mutations affect receptor binding (Figure S1B). This approach measures the effects on binding for mutations that support at least moderate cell entry, and highly deleterious mutations that completely disrupt entry will not yield infectious pseudovirus.

We first tested the neutralization of pseudovirus encoding unmutated RBP by soluble bEFNB2 or bEFNB3. Soluble monomeric and dimeric bENFB2 potently neutralized pseudovirus with half-maximal inhibitory concentrations (IC_{50}) of 0.9 or 0.05 nM, respectively. By contrast, monomeric and dimeric soluble bEFNB3 had IC_{50}s of >400 or 0.6 nM, respectively

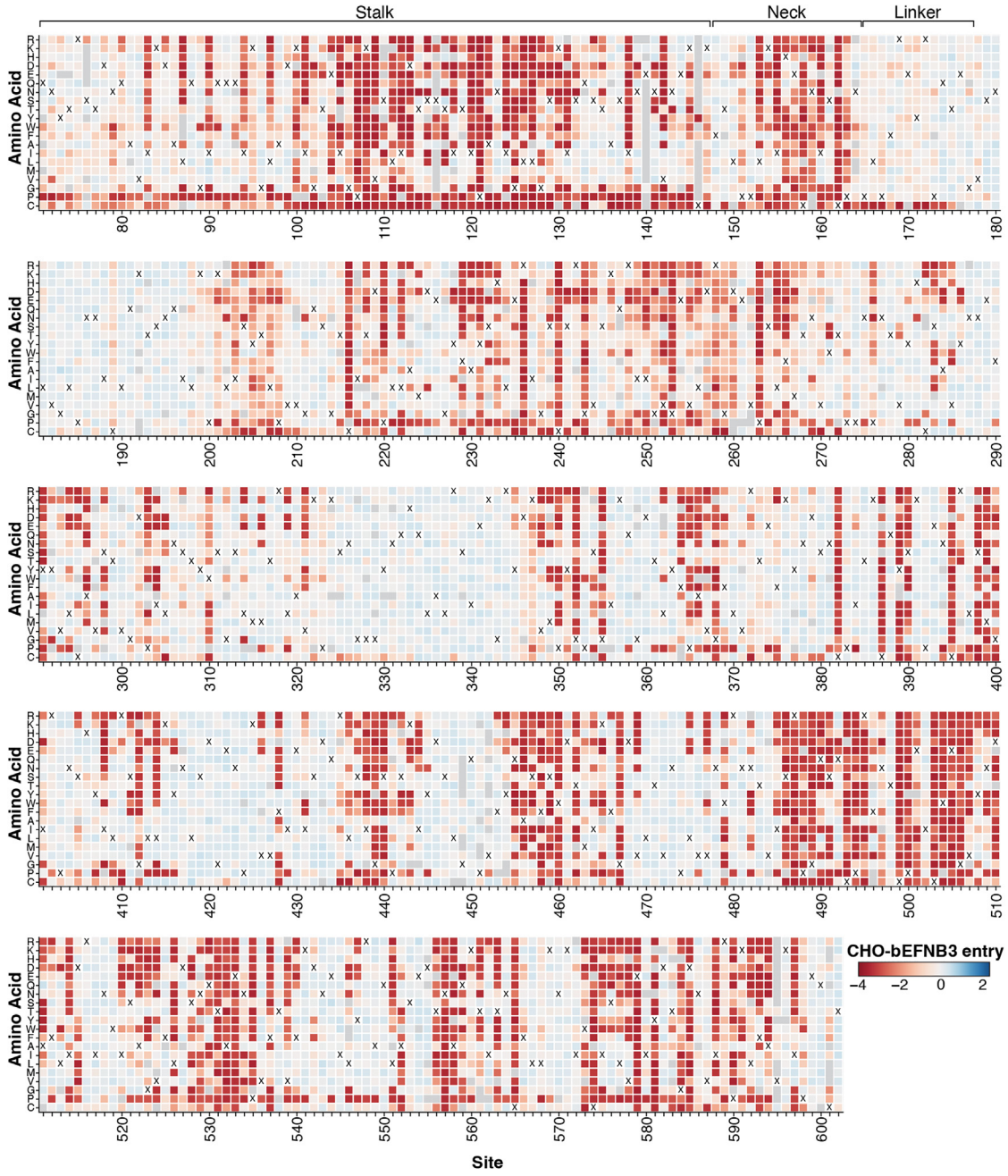

Figure 3. Effects of RBP mutations on entry into CHO-bEFNB3 cells

For each mutation, the entry score reflects the cell entry efficiency (log_2 scale) of a pseudovirus with that RBP mutation relative to the unmutated RBP. Negative values (red) indicate impaired entry, zero (white) indicates no effect, and positive values (blue) indicate improved entry. The wild-type amino acid in the Malaysia strain RBP at each site is indicated with a "X." Mutations that were not measured with high confidence in our experiments are indicated with a light gray box. The stalk, neck, and linker regions are indicated with text above their respective sites, and all other sites are located in the head domain. An interactive version of this heatmap is available at https://dms-vep.org/Nipah_Malaysia_RBP_DMS/htmls/E3_entry_heatmap.html. See https://dms-vep.org/Nipah_Malaysia_RBP_DMS/htmls/E2_entry_heatmap.html for comparable data for cell entry into CHO-bEFNB2 cells.
See also Figure S2.

(Figure 5A). The higher potency of bEFNB2 was expected, given the higher binding affinity of the RBP for EFNB2 relative to EFNB3. We chose to use monomeric bEFNB2 and dimeric bEFNB3 for our DMS library selections due to their similar neutralizing potencies. In total, we measured the effects on binding for 6,672 RBP mutations for bEFNB2 and 6,503 mutations for

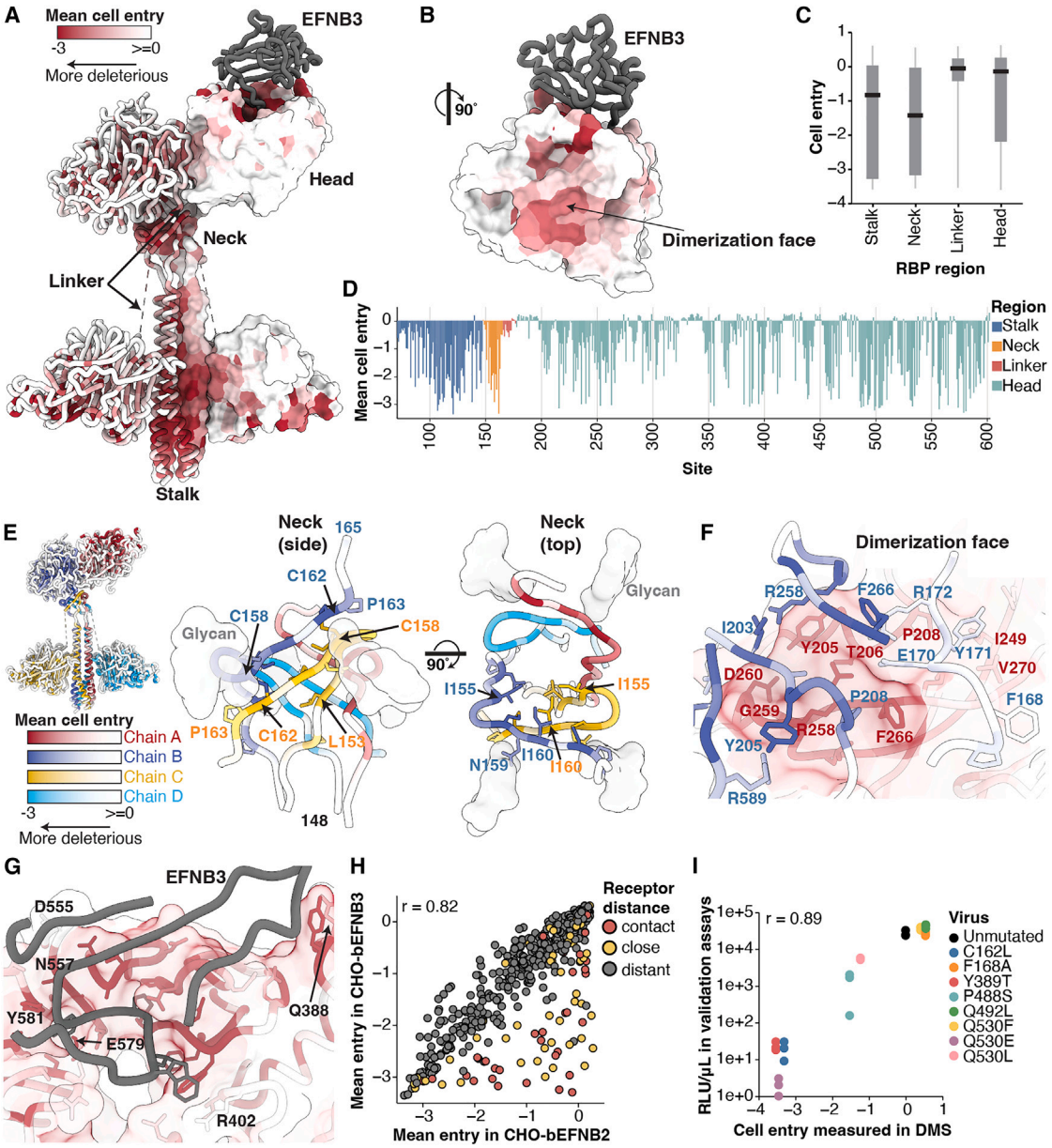

Figure 4. Functional constraint on different regions of RBP for entry into CHO-bEFNB3 cells

(A) RBP tetrameric structure colored by the effect of mutations on cell entry (PDBs: 7TXZ, 7TY0, and 3D12). Each site is colored by the mean effect of all amino-acid mutations at that site, with red indicating impaired cell entry, and white indicating entry comparable to unmutated RBP.

(B) Effects of mutations on cell entry mapped on the RBP head oriented to visualize the RBP dimerization face.

(C) Boxplot showing the impacts of mutations on cell entry across different RBP regions.

(D) Average effects of mutations at each RBP site on cell entry.

(E) Average effect of mutations at each site on cell entry for the RBP neck viewed from the side or top. Each chain has a unique color scale as indicated in the color scale bars, with darker colors indicating impaired entry.

(F) Effects of mutations on entry for the interface between the distal heads (chains A and B).

(G) Effects of mutations on entry at the RBP/EFNB3 interface. The same color scale is used as in (A). EFNB3 is shown as a gray cartoon.

(H) Correlation between effects of mutations on cell entry in CHO-bEFNB2 versus CHO-bEFNB3 cells. Each point is the average effect of mutations at a site. Points are colored by distance to the closest receptor residue (contact sites defined as <4 Å to receptor, close > 4 and < 8 Å, and distant >10 Å).

(I) Validation assays showing the correlation between single-mutant pseudovirus titers in CHO-bEFNB3 cells versus effects measured in DMS. Three independent measurements were made for each validation pseudovirus. Infectivity was quantified by luciferase signal (relative light units [RLU]/µL) at 48 h after infection of CHO-bEFNB3 cells.

See also Figure S2.

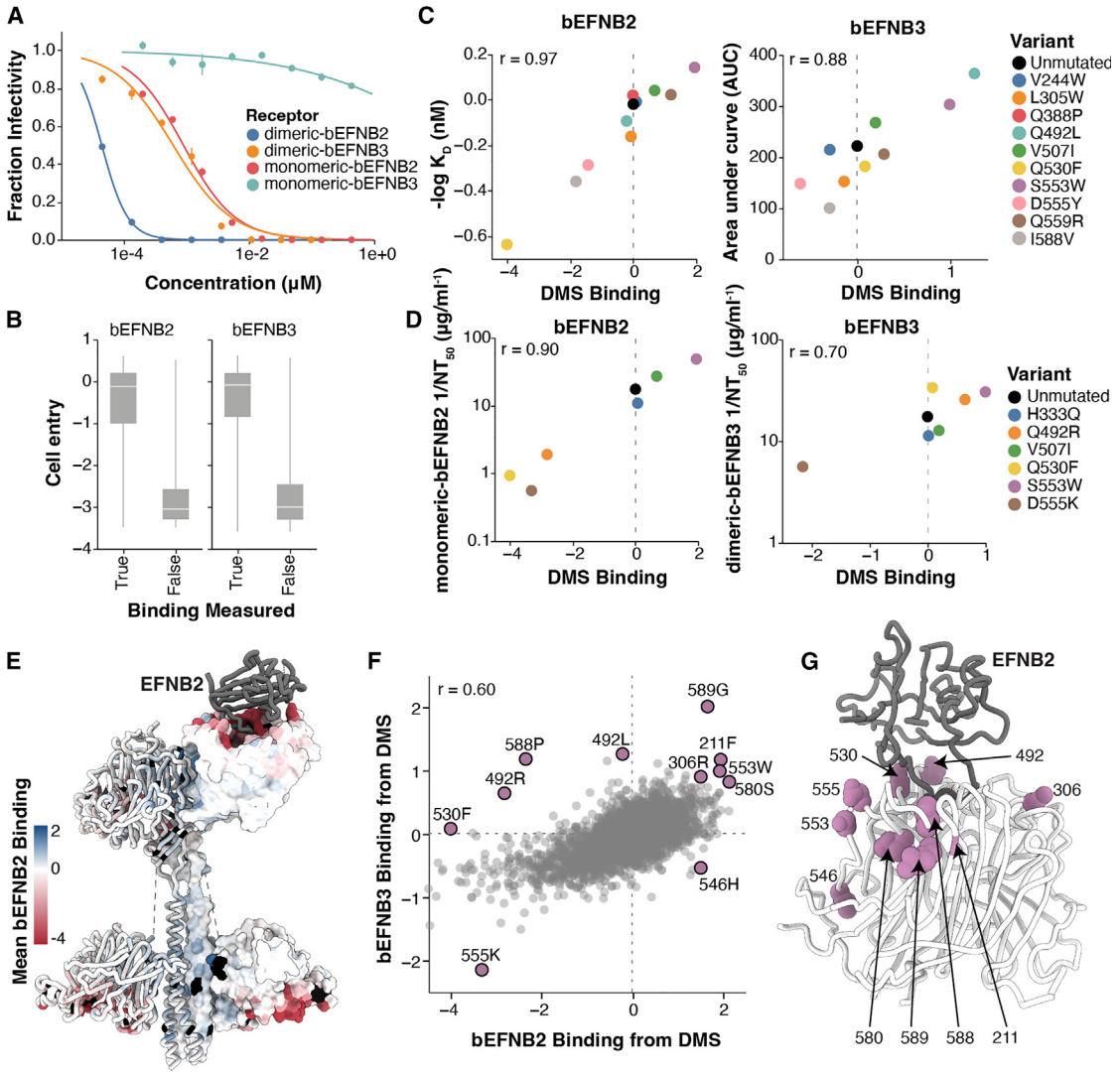

Figure 5. Effects of RBP mutations on binding to bEFNB2 or bEFNB3

(A) Neutralization of unmutated Nipah RBP/F pseudoviruses by monomeric or dimeric soluble bEFNB2 or bEFNB3.

(B) Min-max boxplots showing the distribution of cell entry scores for mutations with and without binding measurements. For bEFNB2, we made binding measurements for 8,257 of the 9,786 mutations with cell entry measurements, and for bEFNB3, we made binding measurements for 7,948 of the 9,713 mutations with cell entry measurements. The reason that we could not make binding measurements for mutations that are highly deleterious for cell entry is that the experimental approach used to measure binding requires the mutant pseudovirus to still be able to infect cells (Figure S1B). However, since the mutations without binding measurements are highly deleterious, they are unlikely to be relevant to actual RBP evolution.

(C) Correlation between biolayer interferometry (BLI) measurements of binding affinity and DMS-measured effects of mutations on binding. The magnitude of binding is shown as $-\log K_D$ for bEFNB2, or the area under the curve (AUC) for bEFNB3 (see Figures S3 and S4A for raw BLI sensorgrams).

(D) Validations in soluble-receptor pseudovirus neutralization assays for key mutations correlate well with DMS. To ensure a positive slope, $1/NT_{50}$ are plotted. The IC_{50} neutralization data for each mutation are in Table S4.

(E) Tetrameric structure of RBP colored by the site-average effects of mutations on binding to bEFNB2. Sites that are missing binding measurements (typically because mutations are highly deleterious for cell entry) are colored black.

(F) Correlation between the effects of mutations on binding to bEFNB2 versus bEFNB3. Mutations with notable effects on binding are labeled.

(G) Location of sites on the RBP head domain that have notable mutations impacting binding. For heatmaps showing the effects of all mutations on binding as measured by DMS, see Figure 6 for links to interactive heatmaps.

See also Figures S3, S4, and S5.

bEFNB3 (Figure 6, see STAR Methods for link to bEFNB3 data). Most mutations for which binding was not measured were highly deleterious for pseudovirus entry (Figure 5B).

To validate that these DMS measurements indeed reflected the strength of RBP binding to bEFNB2/3, we produced the soluble monomeric head domains for ten RBP variants that

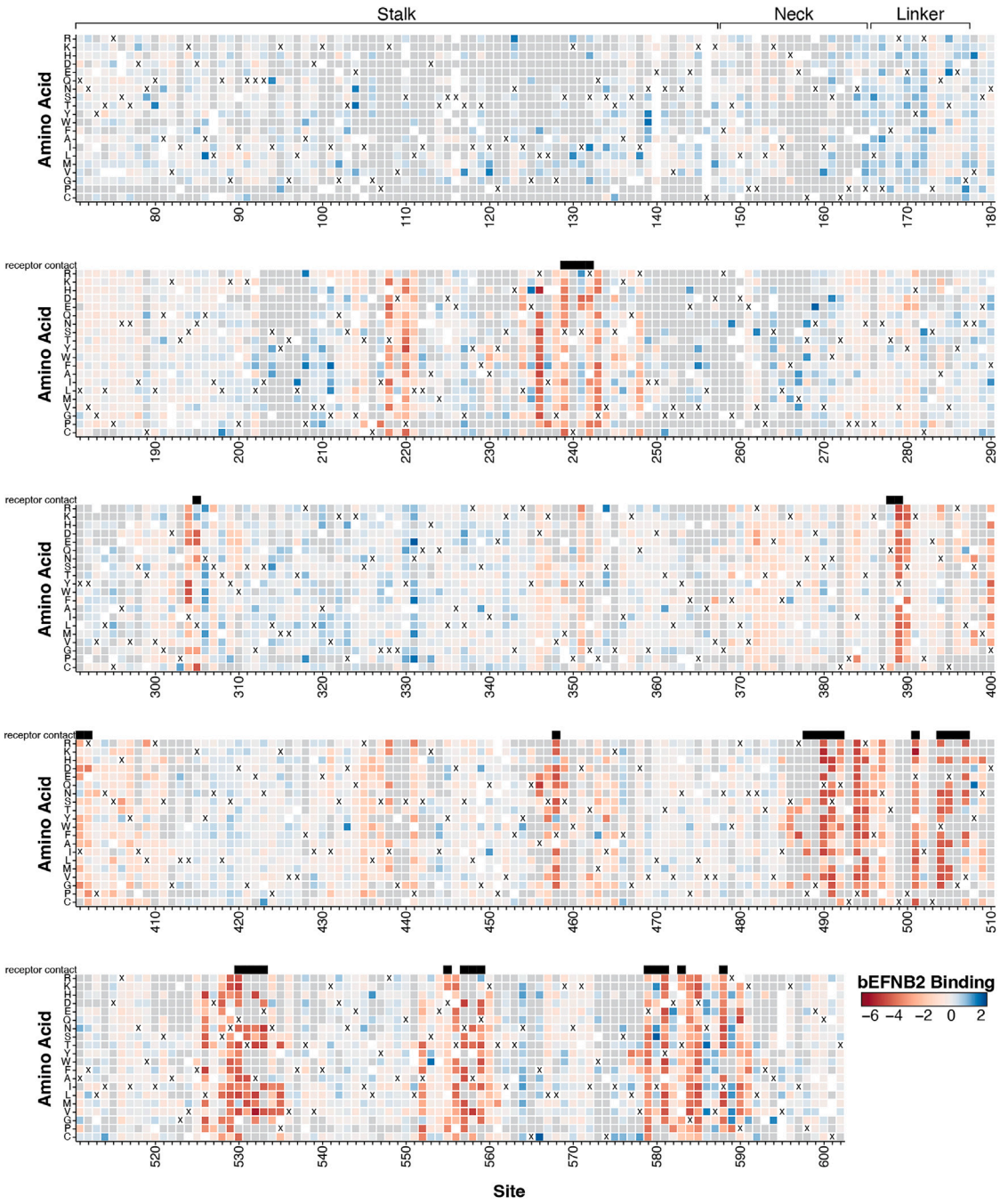

Figure 6. Effects of mutations on binding to monomeric bEFNB2

Mutations that are colored red were neutralized by soluble monomeric bEFNB2 less than the unmutated Nipah RBP (and so have reduced bEFNB2 binding), while mutants colored blue were more neutralized than unmutated (and so have improved bEFNB2 binding). Dark gray squares are mutants that were filtered out due to having a low entry score (<−1.5). White squares are mutations that were missing. Receptor-contact sites are indicated with a black box above the heat map. The amino-acid identity in the parental Malaysia strain RBP at each site is represented with an "X." Sites within the stalk, neck, and linker are labeled, and all remaining sites are located in the head domain. See https://dms-vep.org/Nipah_Malaysia_RBP_DMS/htmls/E2_binding_heatmap.html for an interactive version of this heatmap, and https://dms-vep.org/Nipah_Malaysia_RBP_DMS/htmls/E3_binding_heatmap.html for an interactive heatmap for bEFNB3 binding.
See also Figure S5.

spanned a range of binding effects from DMS and quantified their binding to immobilized bEFNB2 and bEFNB3 using biolayer interferometry (BLI) (Figures 5C, S3, and S4A; Tables S2 and S3). The BLI binding measurements were highly correlated with the DMS measurements (r = 0.97 for bEFNB2; r = 0.88 for bEFNB3; Figure 5C). Although we were able to determine equilibrium dissociation constants (K_D) for bEFNB2 using kinetics fitting of the data, we relied on area under the curve (AUC) to quantify the magnitude of binding for bEFNB3 as explained in the STAR Methods. The RBP mutations tested by BLI did not affect binding to a monoclonal antibody (HENV-32, which recognizes a conformational epitope[20]), demonstrating they are specifically altering receptor binding and not proper head folding (Figure S4B). We also validated that neutralization of six single RBP mutant pseudoviruses by soluble bEFNB2 and bEFNB3 correlated well with the DMS (Figure 5D; Table S4).

Most mutations at receptor-contact sites greatly reduced binding to both bEFNB2 and bEFNB3, whereas mutations across the rest of the RBP had largely neutral effects on binding (Figures 5E, 5F, and 6). Mutations that had opposite effects on binding to bEFNB2 and bEFNB3 were primarily located near the receptor interface (Figures 5F and S5A). Several mutations at site 492 increased binding to bEFNB3 while decreasing binding to bEFNB2 (Figures 5F, 5C, 5D, and S5E). Site 492 is in close proximity to three amino acids in the receptor that differ between bEFNB2 and bEFNB3, and one site that differs between human and bat EFNB2 (Figures S5E and S5F). Several mutations in the loop containing sites 580–590 also had large effects on binding to bEFNB2 versus bEFNB3 (Figures 5G, S5G, and S5H).

Mutations that caused the largest increases in receptor binding were scattered at sites throughout the head (Figure 5G). For instance, S553W increases binding to both bEFNB2 and bEFNB3 even though it does not contact any receptor residues (Figures 5F, 5G, and S5B). This mutation may act by shifting the position of the 580–590 loop or the receptor-contact sites 557–559. G211F increases binding to both bEFNB2 and bEFNB3 and might stabilize the 203–213 loop by favorable van der Waals interactions with I217 and cation-pi interactions with R589 (Figure S5C). Several mutations at site N306, which is glycosylated, also increased binding to both bEFNB2 and bEFNB3 (Figure S5B). These mutations remove the glycan, likely reducing possible steric hindrance of some of the oligosaccharide orientations with receptor engagement (Figure S5D).

We examined the DMS-measured effects of mutations to the Nipah RBP on EFNB2 or EFNB3 for all mutations that differ between Nipah and Hendra RBPs. Most mutations observed in Hendra RBP had neutral effects on binding to bEFNB2 in the Nipah RBP when introduced individually (Figure S5I). Hendra virus mutation R402N decreases binding to bEFNB3 by the Nipah RBP, while two other Hendra virus mutations, F458Y and N586S, increase binding by the Nipah RBP (Figure S5I). These three mutations were present in all Hendra virus RBP sequences relative to Nipah RBP. These results are consistent with Hendra and Nipah virus RBP having similar binding affinity to either EFNB2 or EFNB3.[12,28]

Effects of RBP mutations on antibody escape

We sought to prospectively map how all mutations affected neutralization by six antibodies targeting RBP to define potential escape sites and understand if escape mutations are already circulating or are likely to be tolerated in future evolution. To make these measurements, we incubated the pseudovirus libraries with different concentrations of each antibody, followed by infection of CHO-bEFNB3 target cells, and then deep sequencing to quantify the infection by each RBP mutant relative to a non-neutralizable standard unaffected by the antibody (Figure S1C).

We chose potent neutralizing antibodies that target a diversity of epitopes on the RBP head based on prior structural work or competition mapping studies[20,21,31,46] (Figures S6A–S6C). We measured the IC_{50} for each antibody against unmutated RBP/F pseudovirus, which ranged from 12 to 143 ng/mL (Table S5), consistent with previous studies using authentic virus or a replicating Cedar virus chimera.[20,21,31,32]

Some antibodies were escaped by numerous well-tolerated RBP mutations, whereas others were mostly escaped by mutations that substantially impaired RBP-mediated cell entry (Figure 7A). For example, HENV-103, a dimerization-face-targeting antibody, was escaped primarily at five sites, and most escape mutations at these sites substantially impaired cell entry (Figure 7A). By contrast, nAH1.3 was escaped by mutations at many sites that were well tolerated for cell entry (Figure 7A). These results have implications for antibody countermeasures: for instance, our data suggest there could be a low barrier to resistance to nAH1.3, whereas resistance to HENV-103 may impose a substantial cost on RBP's essential cell-entry function.

The sites of escape for each antibody clustered on the surface of RBP (Figure 7B), near the antibody-binding footprints (Figure S6D). Antibodies m102.4, HENV-26, and HENV-117 all target the receptor-binding face but were mostly escaped by distinct mutations (Figures 7A and 7B). These mutations are at sites mainly along the rim of the receptor pocket, as mutations within the central pocket are likely too deleterious for cell entry to yield functional pseudovirus (Figure 7B; see mutational constraint within the receptor-binding pocket in Figure 4G). The two dimerization-face-targeting antibodies also had slightly different sites of major escape: HENV-103 was escaped primarily at site 205, while HENV-32 was escaped by almost every mutation at site 199, with only minor escape at sites 200 and 205 (Figures 7A and 7B).

Mutations at a subset of sites had opposite effects on antibody neutralization for receptor-binding and dimerization-face-targeting antibodies (Figure S7). For example, mutations at sites 165–172 in the linker region promoted escape from neutralization by receptor-binding face-targeting antibodies while increasing neutralization by dimerization-face-targeting antibodies. These mutations likely alter the conformation of the RBP, which modifies the relative accessibility of each epitope.

Few of the escape mutations identified in our DMS are found in natural Nipah RBP sequences (Figure 7C), consistent with the low diversity of known Nipah isolates. The only notable sequence variations were at sites 172 (escapes receptor-binding face antibodies) and 274 (escapes dimerization-face antibodies), which differ between the two major clades of Nipah virus (Malaysian and Bangladesh; 172R/K, 274P/S, Figure 2A) and could partially explain previously observed differences in certain antibody neutralization potencies between the two strains.[20,21]

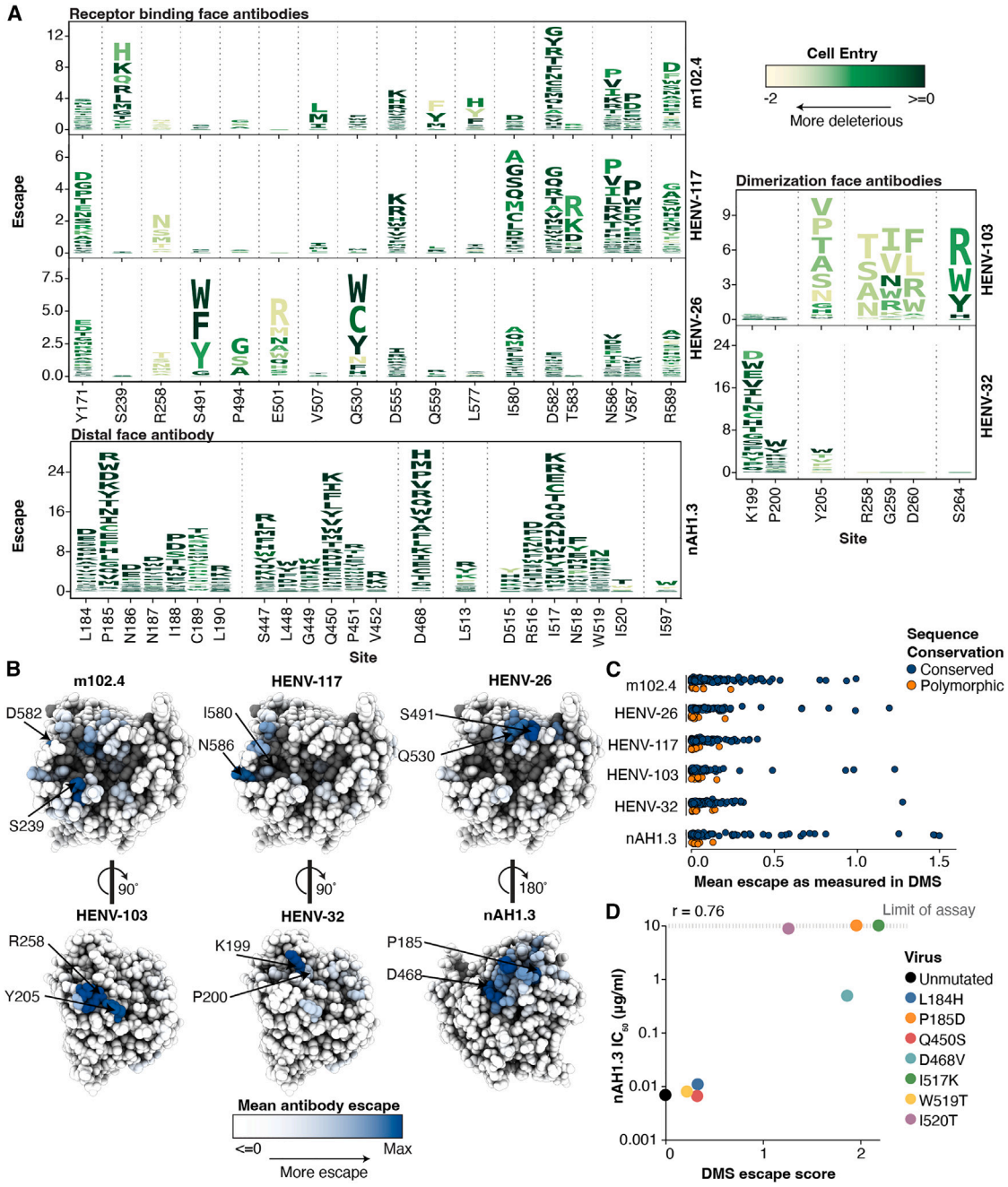

Figure 7. DMS maps of escape mutations from six monoclonal antibodies

(A) Key sites of escape for each antibody. The height of each letter is proportional to the escape caused by that amino-acid mutation, and letters are colored by the effect of that mutation on entry in CHO-bEFNB3 cells (dark green indicates well-tolerated mutations, light yellow indicates impaired cell entry). These logo plots show the top escape sites for each antibody. For all sites, see (https://dms-vep.org/Nipah_Malaysia_RBP_DMS/htmls/mab_plot_all.html). For (A)–(C), only mutations that decrease antibody neutralization are shown.

(B) Antibody escape mapped onto the structure of the RBP head domain. The escape averaged across all mutations at each site is shown as a white-blue color scale, with sites where mutations cause strong escape in darker blue and those not affecting neutralization in white. Dark gray sites have no escape measurements due to mutations strongly impairing cell entry.

(C) Variability of RBP among known Nipah virus isolates at sites of antibody escape mapped in this study. Sites are classified as conserved or polymorphic based on whether they show variation in at least two Nipah RBP sequences.

(D) Correlation between the IC_{50} measured for single-mutant Nipah RBP pseudoviruses for antibody nAH1.3 in validation assays versus escape measured in DMS. The upper limit of IC_{50} values in the validation assays was 10 μg/mL (dashed line).

See also Figures S6 and S7.

Furthermore, mutations present in Hendra virus RBPs did not affect antibody neutralization when introduced in the Nipah RBP (Figure S6E), consistent with previous studies showing similar IC_{50}s between Hendra and Nipah virus for the antibodies examined here.[20,21,31]

To validate the DMS antibody-escape maps, we tested neutralization of seven RBP single mutants in traditional pseudovirus neutralization assays against nAH1.3. The changes in IC_{50} measured in the neutralization assays were highly correlated with the DMS measurements (r = 0.76; Figures 7D and S6F). Escape mutations previously identified using authentic Nipah virus or replicating Cedar virus chimeras also correspond well with our DMS[31] (e.g., I520T introduces an N-linked glycosylation site at position N518 of the RBP within the nAH.1.3 epitope, Table S6).

DISCUSSION

We have measured how all mutations to the Nipah virus RBP affect cell entry, receptor binding, and antibody escape. The resulting maps of mutational effects have important implications both for understanding of Nipah virus cell entry and the design of countermeasures. One major unanswered question is how RBP triggers F following receptor binding, which leads to RBP conformational changes propagating from the RBP head to the neck and stalk to trigger F.[47,48] Our DMS revealed sites in the dimer interface where mutations strongly impair cell entry (e.g., R258 and F266). These sites may be involved in the conformational changes that lead to triggering of F by RBP, though we did not directly measure F-triggering. Dimer interface mutations have been shown to modulate fusion triggering for other paramyxoviruses,[49–51] and molecular dynamics simulations suggested that sites in the Nipah virus RBP dimer interface undergo some of the largest movements following receptor binding.[48] Although the mechanism by which dimer interface sites influence F-triggering is speculative, our results highlight the value of measuring the effects of all mutations in an experimental system that recapitulates the full RBP and F-mediated cell entry process.

Receptor-binding affects both the host range and infectivity of viruses.[52,53] RBP is unusual in strongly binding to two different receptors conserved across six mammalian orders.[15] EFNB2 is broadly expressed in many tissues, while EFNB3 is expressed largely in the brain.[12,54] EFNB2 is likely the key receptor for Nipah virus for transmission, while EFNB3-mediated infection may contribute to the fatal encephalitis and brain pathology frequently observed in human infections.[12] Previous low-throughput mutagenesis experiments found mutations N557S and Y581T severely decreased entry of Nipah pseudovirus in cells expressing EFNB3 relative to EFNB2, while Q559R, T583L, and V587I increased entry in EFNB3-expressing cells relative to EFNB2.[55] Our DMS results are congruent with these findings, while greatly expanding the identification of mutations that alter binding to one versus the other bat versions of these receptors, as well as mutations that increase binding to both bat receptors in a systematic manner.

Antibody therapies against emerging RNA viruses are a powerful approach for treating spillover infections. However, single mutations are often sufficient to escape neutralization and can emerge rapidly.[56,57] Our work prospectively maps all single mutations that escape antibodies while also assessing the impact of those mutations on RBP function, thereby providing a way to assess the potential for resistance mutations to emerge. There was wide variation in how well the mutations that escape different antibodies were tolerated for RBP function. Some antibodies that targeted either the RBP's dimerization or receptor-binding face tended to be escaped mostly by mutations that substantially impaired RBP-mediated cell entry, whereas an antibody targeting the RBP's distal face was escaped by numerous well-tolerated mutations. However, we note that escape mutations that impair cell entry can often be compensated for by additional mutations.[58,59]

Overall, our work defines the functional and antigenic landscape of the Nipah RBP. By measuring how all RBP mutations affect three key protein phenotypes, we define both constraint and plasticity in a way that both informs basic understanding and countermeasures.

Limitations of the study

In this study, we measured the effects of all possible mutations to the Nipah RBP in the context of pseudovirus infection of cell lines, which may differ in some cases from infection of primary cells by authentic virus. For human parainfluenza virus, an RBP mutation that increased fusion in cultured monolayer cells was highly deleterious in human airway epithelium cells, highlighting the complexity of measuring the effects of mutations on viral entry proteins.[50]

We measured the effects of mutations on bEFNB2/3 binding with two different forms, monomeric bEFNB2 and dimeric bEFNB3. Although our results are congruent with previous RBP mutagenesis studies on ephrin binding,[55] distinct conformational changes have been suggested to occur in the Nipah virus RBP following binding to monomeric or dimeric forms of EFNB2.[60] We also used bat EFNB2/3 for all measurements, due to concerns with identifying human-specific adaptations in a potential pandemic virus.[38,39] Mutations may have different effects in the context of human EFNB2/3.

Epistasis can also play a significant role in protein evolution. Although some variants in our DMS libraries contain multiple mutations, the majority of variants contain single mutations, which prohibits us from measuring the extent of epistasis in RBP function. Epistasis has been shown to affect receptor binding in SARS-CoV-2,[61] and compensatory mutations can often emerge during escape from antibodies or sera.[58,59] Therefore, although we measured the effects of single mutations on cell entry, receptor binding, and antibody escape, our results do not capture the full evolutionary landscape available to the RBP due to the confounding role of epistasis. Despite these caveats, our results from a representative Nipah virus represent a useful resource for the scientific community, as demonstrated for SARS-CoV-2 during the COVID-19 pandemic.[62]

RESOURCE AVAILABILITY

Lead contact

Requests for reagents and resources should be directed to the lead contact, Jesse Bloom (jbloom@fredhutch.org).

Materials availability

Products generated by this study are available upon request.

Data and code availability

All raw data and code used for data analysis are publicly available here: https://github.com/dms-vep/Nipah_Malaysia_RBP_DMS. A landing page with links to Jupyter notebooks, raw data, and interactive visualizations is available here: https://dms-vep.org/Nipah_Malaysia_RBP_DMS/. Raw sequencing reads have been deposited in NCBI SRA under BioProject PRJNA1194132.

ACKNOWLEDGMENTS

We thank Bernadeta Dadonaite for helpful advice during the course of this project. We also thank Stacey Rutherford at Vanderbilt for technical support in monoclonal antibody production. This research was also supported by the Genomics & Bioinformatics Shared Resource (RRID: SCR_022606) and the Flow Cytometry Shared Resource (RRID: SCR_022613) of the Fred Hutch/University of Washington/Seattle Children's Cancer Consortium (P30 CA015704), as well as by Fred Hutch Scientific Computing, and NIH grants S10-OD-020069 and S10-OD-028685. Funding: this work was supported in part by the NIH/NIAID under grants R01AI141707 to J.D.B., 1U19AI181881 to J.D.B. and D.V., DP1AI158186 and 75N93022C00036 to D.V., and a project in grant U19 AI142764 to J.E.C. It was also supported by an Investigators in the Pathogenesis of Infectious Disease Awards from the Burroughs Wellcome Fund (to D.V.), the University of Washington Arnold and Mabel Beckman Cryo-EM Center, and the National Institute of Health grant S10OD032290 (to D.V.). J.D.B. and D.V. are investigators of the Howard Hughes Medical Institute, and D.V. holds the Hans Neurath Endowed Chair in Biochemistry at the University of Washington. B.B.L. is a Washington Research Foundation postdoctoral fellow.

AUTHOR CONTRIBUTIONS

Conceptualization, B.B.L. and J.D.B.; data curation, B.B.L., J.T.B., D.V., and J.D.B.; formal analysis, B.B.L., D.V., and J.D.B.; funding acquisition, J.D.B. and D.V.; investigation, B.B.L., T.M., Z.W., and J.T.B.; methodology, J.D.B., B.B.L., T.M., and C.E.R.; project administration, J.D.B. and D.V.; resources, D.V., Z.W., J.T.B., J.E.C.; software, J.D.B. and B.B.L.; supervision, J.D.B. and D.V.; validation, B.B.L. and T.M.; visualization, B.B.L. and J.D.B.; writing – original draft, B.B.L. and J.D.B.; writing – review and editing, J.D.B., B.B.L., and D.V.

DECLARATION OF INTERESTS

J.D.B. is on the scientific advisory boards of Apriori Bio, Invivyd, and the Vaccine Company. J.D.B. consults for GlaxoSmithKline and Pfizer. J.D.B. receives royalty payments as an inventor on Fred Hutch-licensed patents related to viral DMS. J.E.C. has served as a consultant for Luna Labs USA, Merck Sharp & Dohme Corporation, Emergent Biosolutions, GlaxoSmithKline, and BTG International Inc. J.E.C. is a member of the scientific advisory board of Meissa Vaccines, a former member of the Scientific Advisory Board of Gigagen (Grifols), and is founder of IDBiologics. The laboratory of J.E.C. received unrelated sponsored research agreements from AstraZeneca, Takeda, and IDBiologics during the conduct of the study. Vanderbilt University has applied for a patent pertinent to some of the materials in this paper.

STAR★METHODS

Detailed methods are provided in the online version of this paper and include the following:

- KEY RESOURCES TABLE
- METHOD DETAILS
  - Data availability and interactive plots of results
  - Plasmid maps and primer sequences
  - Creation of CHO-bEFNB2 and CHO-bEFNB3 target cells
  - Anti-RBP monoclonal antibodies
  - Lentivirus backbone for RBP deep mutational scanning
  - RBP mutant library design and production
  - Rescue of RBP pseudovirus library from transfection and creation of cell-stored mutant library
  - Rescue of RBP and F expressing pseudoviruses from cell-stored mutant library
  - Long-read sequencing to link mutations to barcodes
  - Extraction of lentiviral episomal DNA
  - Illumina barcode sequencing
  - Validations of DMS data using single mutant Nipah pseudoviruses
  - Production of a VSV-neutralization standard virus
  - Selections to determine effects of mutations on cell entry
  - Selections to determine effects of mutations on receptor binding
  - Selections to determine effects of mutations on antibody neutralization
  - Data filtering
  - Validation of RBP binding measurements by biolayer interferometry
  - Nipah virus RBP recombinant production
  - Monomeric *Pteropus alecto* Ephrin-B2 and -B3 purification
  - *Pteropus alecto* Ephrin B2-hFc and B3-hFc production
  - Logo plots
  - Structural analyses
  - Sequence analysis
  - Figures

SUPPLEMENTAL INFORMATION

Supplemental information can be found online at https://doi.org/10.1016/j.cell.2025.02.030.

Received: May 8, 2024
Revised: December 30, 2024
Accepted: February 25, 2025
Published: March 24, 2025

REFERENCES

1. Chua, K.B., Bellini, W.J., Rota, P.A., Harcourt, B.H., Tamin, A., Lam, S.K., Ksiazek, T.G., Rollin, P.E., Zaki, S.R., Shieh, W., et al. (2000). Nipah virus: a recently emergent deadly paramyxovirus. Science *288*, 1432–1435. https://doi.org/10.1126/science.288.5470.1432.
2. Chua, K.B., Koh, C.L., Hooi, P.S., Wee, K.F., Khong, J.H., Chua, B.H., Chan, Y.P., Lim, M.E., and Lam, S.K. (2002). Isolation of Nipah virus from Malaysian Island flying-foxes. Microbes Infect. *4*, 145–151. https://doi.org/10.1016/s1286-4579(01)01522-2.
3. Epstein, J.H., Prakash, V., Smith, C.S., Daszak, P., McLaughlin, A.B., Meehan, G., Field, H.E., and Cunningham, A.A. (2008). Henipavirus infection in fruit bats (Pteropus giganteus), India. Emerg. Infect. Dis. *14*, 1309–1311. https://doi.org/10.3201/eid1408.071492.
4. Epstein, J.H., Anthony, S.J., Islam, A., Kilpatrick, A.M., Ali Khan, S., Balkey, M.D., Ross, N., Smith, I., Zambrana-Torrelio, C., Tao, Y., et al. (2020). Nipah virus dynamics in bats and implications for spillover to humans. Proc. Natl. Acad. Sci. USA *117*, 29190–29201. https://doi.org/10.1073/pnas.2000429117.
5. Epstein, J.H., Field, H.E., Luby, S., Pulliam, J.R.C., and Daszak, P. (2006). Nipah virus: impact, origins, and causes of emergence. Curr. Infect. Dis. Rep. *8*, 59–65. https://doi.org/10.1007/s11908-006-0036-2.
6. Wong, K.T., Shieh, W.-J., Kumar, S., Norain, K., Abdullah, W., Guarner, J., Goldsmith, C.S., Chua, K.B., Lam, S.K., Tan, C.T., et al. (2002). Nipah virus infection: pathology and pathogenesis of an emerging paramyxoviral zoonosis. Am. J. Pathol. *161*, 2153–2167. https://doi.org/10.1016/S0002-9440(10)64493-8.
7. Kaza, B., and Aguilar, H.C. (2023). Pathogenicity and virulence of henipaviruses. Virulence *14*, 2273684. https://doi.org/10.1080/21505594.2023.2273684.

8. Gurley, E.S., Montgomery, J.M., Hossain, M.J., Bell, M., Azad, A.K., Islam, M.R., Molla, M.A.R., Carroll, D.S., Ksiazek, T.G., Rota, P.A., et al. (2007). Person-to-person transmission of Nipah virus in a Bangladeshi community. Emerg. Infect. Dis. *13*, 1031–1037. https://doi.org/10.3201/eid1307.061128.

9. Nikolay, B., Salje, H., Hossain, M.J., Khan, A.K.M.D., Sazzad, H.M.S., Rahman, M., Daszak, P., Ströher, U., Pulliam, J.R.C., Kilpatrick, A.M., et al. (2019). Transmission of Nipah Virus - 14 Years of Investigations in Bangladesh. N. Engl. J. Med. *380*, 1804–1814. https://doi.org/10.1056/NEJMoa1805376.

10. Bonaparte, M.I., Dimitrov, A.S., Bossart, K.N., Crameri, G., Mungall, B.A., Bishop, K.A., Choudhry, V., Dimitrov, D.S., Wang, L.-F., Eaton, B.T., et al. (2005). Ephrin-B2 ligand is a functional receptor for Hendra virus and Nipah virus. Proc. Natl. Acad. Sci. USA *102*, 10652–10657. https://doi.org/10.1073/pnas.0504887102.

11. Negrete, O.A., Levroney, E.L., Aguilar, H.C., Bertolotti-Ciarlet, A., Nazarian, R., Tajyar, S., and Lee, B. (2005). EphrinB2 is the entry receptor for Nipah virus, an emergent deadly paramyxovirus. Nature *436*, 401–405. https://doi.org/10.1038/nature03838.

12. Negrete, O.A., Chu, D., Aguilar, H.C., and Lee, B. (2007). Single amino acid changes in the Nipah and Hendra virus attachment glycoproteins distinguish ephrinB2 from ephrinB3 usage. J. Virol. *81*, 10804–10814. https://doi.org/10.1128/JVI.00999-07.

13. Negrete, O.A., Wolf, M.C., Aguilar, H.C., Enterlein, S., Wang, W., Mühlberger, E., Su, S.V., Bertolotti-Ciarlet, A., Flick, R., and Lee, B. (2006). Two key residues in ephrinB3 are critical for its use as an alternative receptor for Nipah virus. PLoS Pathog. *2*, e7. https://doi.org/10.1371/journal.ppat.0020007.

14. Poliakov, A., Cotrina, M., and Wilkinson, D.G. (2004). Diverse roles of eph receptors and ephrins in the regulation of cell migration and tissue assembly. Dev. Cell *7*, 465–480. https://doi.org/10.1016/j.devcel.2004.09.006.

15. Bossart, K.N., Tachedjian, M., McEachern, J.A., Crameri, G., Zhu, Z., Dimitrov, D.S., Broder, C.C., and Wang, L.-F. (2008). Functional studies of host-specific ephrin-B ligands as Henipavirus receptors. Virology *372*, 357–371. https://doi.org/10.1016/j.virol.2007.11.011.

16. Pernet, O., Wang, Y.E., and Lee, B. (2012). Henipavirus receptor usage and tropism. Curr. Top. Microbiol. Immunol. *359*, 59–78. https://doi.org/10.1007/82_2012_222.

17. Liu, Q., Stone, J.A., Bradel-Tretheway, B., Dabundo, J., Benavides Montano, J.A., Santos-Montanez, J., Biering, S.B., Nicola, A.V., Iorio, R.M., Lu, X., et al. (2013). Unraveling a three-step spatiotemporal mechanism of triggering of receptor-induced Nipah virus fusion and cell entry. PLoS Pathog. *9*, e1003770. https://doi.org/10.1371/journal.ppat.1003770.

18. Bossart, K.N., Zhu, Z., Middleton, D., Klippel, J., Crameri, G., Bingham, J., McEachern, J.A., Green, D., Hancock, T.J., Chan, Y.-P., et al. (2009). A neutralizing human monoclonal antibody protects against lethal disease in a new ferret model of acute Nipah virus infection. PLoS Pathog. *5*, e1000642. https://doi.org/10.1371/journal.ppat.1000642.

19. Geisbert, T.W., Mire, C.E., Geisbert, J.B., Chan, Y.-P., Agans, K.N., Feldmann, F., Fenton, K.A., Zhu, Z., Dimitrov, D.S., Scott, D.P., et al. (2014). Therapeutic treatment of Nipah virus infection in nonhuman primates with a neutralizing human monoclonal antibody. Sci. Transl. Med. *6*, 242ra82. https://doi.org/10.1126/scitranslmed.3008929.

20. Dong, J., Cross, R.W., Doyle, M.P., Kose, N., Mousa, J.J., Annand, E.J., Borisevich, V., Agans, K.N., Sutton, R., Nargi, R., et al. (2020). Potent Henipavirus Neutralization by Antibodies Recognizing Diverse Sites on Hendra and Nipah Virus Receptor Binding Protein. Cell *183*, 1536–1550.e17. https://doi.org/10.1016/j.cell.2020.11.023.

21. Doyle, M.P., Kose, N., Borisevich, V., Binshtein, E., Amaya, M., Nagel, M., Annand, E.J., Armstrong, E., Bombardi, R., Dong, J., et al. (2021). Cooperativity mediated by rationally selected combinations of human monoclonal antibodies targeting the henipavirus receptor binding protein. Cell Rep. *36*, 109628. https://doi.org/10.1016/j.celrep.2021.109628.

22. de Wit, E., Feldmann, F., Cronin, J., Goldin, K., Mercado-Hernandez, R., Williamson, B.N., Meade-White, K., Okumura, A., Callison, J., Weatherman, S., et al. (2023). Distinct VSV-based Nipah virus vaccines expressing either glycoprotein G or fusion protein F provide homologous and heterologous protection in a nonhuman primate model. EBiomedicine *87*, 104405. https://doi.org/10.1016/j.ebiom.2022.104405.

23. Foster, S.L., Woolsey, C., Borisevich, V., Agans, K.N., Prasad, A.N., Deer, D.J., Geisbert, J.B., Dobias, N.S., Fenton, K.A., Cross, R.W., et al. (2022). A recombinant VSV-vectored vaccine rapidly protects nonhuman primates against lethal Nipah virus disease. Proc. Natl. Acad. Sci. USA *119*, e2200065119. https://doi.org/10.1073/pnas.2200065119.

24. Geisbert, T.W., Bobb, K., Borisevich, V., Geisbert, J.B., Agans, K.N., Cross, R.W., Prasad, A.N., Fenton, K.A., Yu, H., Fouts, T.R., et al. (2021). A single dose investigational subunit vaccine for human use against Nipah virus and Hendra virus. NPJ Vaccines *6*, 23. https://doi.org/10.1038/s41541-021-00284-w.

25. DeBuysscher, B.L., Scott, D., Marzi, A., Prescott, J., and Feldmann, H. (2014). Single-dose live-attenuated Nipah virus vaccines confer complete protection by eliciting antibodies directed against surface glycoproteins. Vaccine *32*, 2637–2644. https://doi.org/10.1016/j.vaccine.2014.02.087.

26. Prescott, J., DeBuysscher, B.L., Feldmann, F., Gardner, D.J., Haddock, E., Martellaro, C., Scott, D., and Feldmann, H. (2015). Single-dose live-attenuated vesicular stomatitis virus-based vaccine protects African green monkeys from Nipah virus disease. Vaccine *33*, 2823–2829. https://doi.org/10.1016/j.vaccine.2015.03.089.

27. Zeitlin, L., Cross, R.W., Woolsey, C., West, B.R., Borisevich, V., Agans, K.N., Prasad, A.N., Deer, D.J., Stuart, L., McCavitt-Malvido, M., et al. (2024). Therapeutic administration of a cross-reactive mAb targeting the fusion glycoprotein of Nipah virus protects nonhuman primates. Sci. Transl. Med. *16*, eadl2055. https://doi.org/10.1126/scitranslmed.adl2055.

28. Wang, Z., Dang, H.V., Amaya, M., Xu, Y., Yin, R., Yan, L., Hickey, A.C., Annand, E.J., Horsburgh, B.A., Reid, P.A., et al. (2022). Potent monoclonal antibody-mediated neutralization of a divergent Hendra virus variant. Proc. Natl. Acad. Sci. USA *119*, e2122769119. https://doi.org/10.1073/pnas.2122769119.

29. Dang, H.V., Cross, R.W., Borisevich, V., Bornholdt, Z.A., West, B.R., Chan, Y.-P., Mire, C.E., Da Silva, S.C., Dimitrov, A.S., Yan, L., et al. (2021). Broadly neutralizing antibody cocktails targeting Nipah virus and Hendra virus fusion glycoproteins. Nat. Struct. Mol. Biol. *28*, 426–434. https://doi.org/10.1038/s41594-021-00584-8.

30. VanBlargan, L.A., Errico, J.M., Halfmann, P.J., Zost, S.J., Crowe, J.E., Jr., Purcell, L.A., Kawaoka, Y., Corti, D., Fremont, D.H., and Diamond, M.S. (2022). An infectious SARS-CoV-2 B.1.1.529 Omicron virus escapes neutralization by therapeutic monoclonal antibodies. Nat. Med. *28*, 490–495. https://doi.org/10.1038/s41591-021-01678-y.

31. Wang, Z., Amaya, M., Addetia, A., Dang, H.V., Reggiano, G., Yan, L., Hickey, A.C., DiMaio, F., Broder, C.C., and Veesler, D. (2022). Architecture and antigenicity of the Nipah virus attachment glycoprotein. Science *375*, 1373–1378. https://doi.org/10.1126/science.abm5561.

32. Borisevich, V., Lee, B., Hickey, A., DeBuysscher, B., Broder, C.C., Feldmann, H., and Rockx, B. (2016). Escape From Monoclonal Antibody Neutralization Affects Henipavirus Fitness In Vitro and In Vivo. J. Infect. Dis. *213*, 448–455. https://doi.org/10.1093/infdis/jiv449.

33. Dadonaite, B., Crawford, K.H.D., Radford, C.E., Farrell, A.G., Yu, T.C., Hannon, W.W., Zhou, P., Andrabi, R., Burton, D.R., Liu, L., et al. (2023). A pseudovirus system enables deep mutational scanning of the full SARS-CoV-2 spike. Cell *186*, 1263–1278.e20. https://doi.org/10.1016/j.cell.2023.02.001.

34. Radford, C.E., Schommers, P., Gieselmann, L., Crawford, K.H.D., Dadonaite, B., Yu, T.C., Dingens, A.S., Overbaugh, J., Klein, F., and Bloom, J.D. (2023). Mapping the neutralizing specificity of human anti-HIV serum by deep mutational scanning. Cell Host Microbe *31*, 1200–1215.e9. https://doi.org/10.1016/j.chom.2023.05.025.

35. Khetawat, D., and Broder, C.C. (2010). A functional henipavirus envelope glycoprotein pseudotyped lentivirus assay system. Virol. J. *7*, 312. https://doi.org/10.1186/1743-422X-7-312.

36. Witting, S.R., Vallanda, P., and Gamble, A.L. (2013). Characterization of a third generation lentiviral vector pseudotyped with Nipah virus envelope proteins for endothelial cell transduction. Gene Ther. *20*, 997–1005. https://doi.org/10.1038/gt.2013.23.

37. Field, H., de Jong, C., Melville, D., Smith, C., Smith, I., Broos, A., Kung, Y.H.N., McLaughlin, A., and Zeddeman, A. (2011). Hendra virus infection dynamics in Australian fruit bats. PLoS One *6*, e28678. https://doi.org/10.1371/journal.pone.0028678.

38. Esvelt, K.M. (2018). Inoculating science against potential pandemics and information hazards. PLoS Pathog. *14*, e1007286. https://doi.org/10.1371/journal.ppat.1007286.

39. Lewis, G., Millett, P., Sandberg, A., Snyder-Beattie, A., and Gronvall, G. (2019). Information Hazards in Biotechnology. Risk Anal. *39*, 975–981. https://doi.org/10.1111/risa.13235.

40. Otwinowski, J., McCandlish, D.M., and Plotkin, J.B. (2018). Inferring the shape of global epistasis. Proc. Natl. Acad. Sci. USA *115*, E7550–E7558. https://doi.org/10.1073/pnas.1804015115.

41. Maar, D., Harmon, B., Chu, D., Schulz, B., Aguilar, H.C., Lee, B., and Negrete, O.A. (2012). Cysteines in the stalk of the nipah virus G glycoprotein are located in a distinct subdomain critical for fusion activation. J. Virol. *86*, 6632–6642. https://doi.org/10.1128/JVI.00076-12.

42. Biering, S.B., Huang, A., Vu, A.T., Robinson, L.R., Bradel-Tretheway, B., Choi, E., Lee, B., and Aguilar, H.C. (2012). N-Glycans on the Nipah virus attachment glycoprotein modulate fusion and viral entry as they protect against antibody neutralization. J. Virol. *86*, 11991–12002. https://doi.org/10.1128/JVI.01304-12.

43. Wang, Q., Iketani, S., Li, Z., Guo, Y., Yeh, A.Y., Liu, M., Yu, J., Sheng, Z., Huang, Y., Liu, L., et al. (2022). Antigenic characterization of the SARS-CoV-2 Omicron subvariant BA.2.75. Cell Host Microbe *30*, 1512–1517.e4. https://doi.org/10.1016/j.chom.2022.09.002.

44. Cao, Y., Jian, F., Wang, J., Yu, Y., Song, W., Yisimayi, A., Wang, J., An, R., Chen, X., Zhang, N., et al. (2023). Imprinted SARS-CoV-2 humoral immunity induces convergent Omicron RBD evolution. Nature *614*, 521–529. https://doi.org/10.1038/s41586-022-05644-7.

45. Tortorici, M.A., Walls, A.C., Joshi, A., Park, Y.-J., Eguia, R.T., Miranda, M.C., Kepl, E., Dosey, A., Stevens-Ayers, T., Boeckh, M.J., et al. (2022). Structure, receptor recognition, and antigenicity of the human coronavirus CCoV-HuPn-2018 spike glycoprotein. Cell *185*, 2279–2291.e17. https://doi.org/10.1016/j.cell.2022.05.019.

46. Xu, K., Rockx, B., Xie, Y., DeBuysscher, B.L., Fusco, D.L., Zhu, Z., Chan, Y.-P., Xu, Y., Luu, T., Cer, R.Z., et al. (2013). Crystal structure of the Hendra virus attachment G glycoprotein bound to a potent cross-reactive neutralizing human monoclonal antibody. PLoS Pathog. *9*, e1003684. https://doi.org/10.1371/journal.ppat.1003684.

47. Aguilar, H.C., Ataman, Z.A., Aspericueta, V., Fang, A.Q., Stroud, M., Negrete, O.A., Kammerer, R.A., and Lee, B. (2009). A novel receptor-induced activation site in the Nipah virus attachment glycoprotein (G) involved in triggering the fusion glycoprotein (F). J. Biol. Chem. *284*, 1628–1635. https://doi.org/10.1074/jbc.M807469200.

48. Dutta, P., Siddiqui, A., Botlani, M., and Varma, S. (2016). Stimulation of Nipah Fusion: Small Intradomain Changes Trigger Extensive Interdomain Rearrangements. Biophys. J. *111*, 1621–1630. https://doi.org/10.1016/j.bpj.2016.09.002.

49. Iketani, S., Shean, R.C., Ferren, M., Makhsous, N., Aquino, D.B., des Georges, A., Rima, B., Mathieu, C., Porotto, M., Moscona, A., et al. (2018). Viral entry properties required for fitness in humans are lost through rapid genomic change during viral isolation. mBio *9*, e0089818. https://doi.org/10.1128/mBio.00898-18.

50. Xu, R., Palmer, S.G., Porotto, M., Palermo, L.M., Niewiesk, S., Wilson, I.A., and Moscona, A. (2013). Interaction between the hemagglutinin-neuraminidase and fusion glycoproteins of human Parainfluenza virus type III regulates viral growth *in vivo*. mBio *4*, e00803–e00813. https://doi.org/10.1128/mBio.00803-13.

51. Nakashima, M., Shirogane, Y., Hashiguchi, T., and Yanagi, Y. (2013). Mutations in the putative dimer-dimer interfaces of the measles virus hemagglutinin head domain affect membrane fusion triggering. J. Biol. Chem. *288*, 8085–8091. https://doi.org/10.1074/jbc.M112.427609.

52. Starr, T.N., Zepeda, S.K., Walls, A.C., Greaney, A.J., Alkhovsky, S., Veesler, D., and Bloom, J.D. (2022). ACE2 binding is an ancestral and evolvable trait of sarbecoviruses. Nature *603*, 913–918. https://doi.org/10.1038/s41586-022-04464-z.

53. de Graaf, M., and Fouchier, R.A.M. (2014). Role of receptor binding specificity in influenza A virus transmission and pathogenesis. EMBO J. *33*, 823–841. https://doi.org/10.1002/embj.201387442.

54. Bergemann, A.D., Zhang, L., Chiang, M.K., Brambilla, R., Klein, R., and Flanagan, J.G. (1998). Ephrin-B3, a ligand for the receptor EphB3, expressed at the midline of the developing neural tube. Oncogene *16*, 471–480. https://doi.org/10.1038/sj.onc.1201557.

55. Oguntuyo, K.Y., Haas, G.D., Azarm, K.D., Stevens, C.S., Brambilla, L., Kowdle, S.S., Avanzato, V.A., Pryce, R., Freiberg, A.N., Bowden, T.A., et al. (2024). Structure-guided mutagenesis of Henipavirus receptor-binding proteins reveals molecular determinants of receptor usage and antibody-binding epitopes. J. Virol. *98*, e0183823. https://doi.org/10.1128/jvi.01838-23.

56. Starr, T.N., Greaney, A.J., Addetia, A., Hannon, W.W., Choudhary, M.C., Dingens, A.S., Li, J.Z., and Bloom, J.D. (2021). Prospective mapping of viral mutations that escape antibodies used to treat COVID-19. Science *371*, 850–854. https://doi.org/10.1126/science.abf9302.

57. Burke, C.W., Froude, J.W., Rossi, F., White, C.E., Moyer, C.L., Ennis, J., Pitt, M.L., Streatfield, S., Jones, R.M., Musiychuk, K., et al. (2019). Therapeutic monoclonal antibody treatment protects nonhuman primates from severe Venezuelan equine encephalitis virus disease after aerosol exposure. PLoS Pathog. *15*, e1008157. https://doi.org/10.1371/journal.ppat.1008157.

58. Myers, J.L., Wetzel, K.S., Linderman, S.L., Li, Y., Sullivan, C.B., and Hensley, S.E. (2013). Compensatory hemagglutinin mutations alter antigenic properties of influenza viruses. J. Virol. *87*, 11168–11172. https://doi.org/10.1128/JVI.01414-13.

59. Moulana, A., Dupic, T., Phillips, A.M., Chang, J., Nieves, S., Roffler, A.A., Greaney, A.J., Starr, T.N., Bloom, J.D., and Desai, M.M. (2022). Compensatory epistasis maintains ACE2 affinity in SARS-CoV-2 Omicron BA.1. Nat. Commun. *13*, 7011. https://doi.org/10.1038/s41467-022-34506-z.

60. Wong, J.J.W., Young, T.A., Zhang, J., Liu, S., Leser, G.P., Komives, E.A., Lamb, R.A., Zhou, Z.H., Salafsky, J., and Jardetzky, T.S. (2017). Monomeric ephrinB2 binding induces allosteric changes in Nipah virus G that precede its full activation. Nat. Commun. *8*, 781. https://doi.org/10.1038/s41467-017-00863-3.

61. Starr, T.N., Greaney, A.J., Hannon, W.W., Loes, A.N., Hauser, K., Dillen, J.R., Ferri, E., Farrell, A.G., Dadonaite, B., McCallum, M., et al. (2022). Shifting mutational constraints in the SARS-CoV-2 receptor-binding domain during viral evolution. Science *377*, 420–424. https://doi.org/10.1126/science.abo7896.

62. Starr, T.N., Greaney, A.J., Hilton, S.K., Ellis, D., Crawford, K.H.D., Dingens, A.S., Navarro, M.J., Bowen, J.E., Tortorici, M.A., Walls, A.C., et al. (2020). Deep Mutational Scanning of SARS-CoV-2 Receptor Binding Domain Reveals Constraints on Folding and ACE2 Binding. Cell *182*, 1295–1310.e20. https://doi.org/10.1016/j.cell.2020.08.012.

63. Crawford, K.H.D., and Bloom, J.D. (2019). alignparse: A Python package for parsing complex features from high-throughput long-read sequencing. J. Open Source Softw. *4*, 1915. https://doi.org/10.21105/joss.01915.

64. Loes, A.N., Tarabi, R.A.L., Huddleston, J., Touyon, L., Wong, S.S., Cheng, S.M.S., Leung, N.H.L., Hannon, W.W., Bedford, T., Cobey, S., et al. (2024). High-throughput sequencing-based neutralization assay reveals how

repeated vaccinations impact titers to recent human H1N1 influenza strains. J. Virol. *98*, e00689-24. https://doi.org/10.1128/jvi.00689-24.

65. Yu, T.C., Thornton, Z.T., Hannon, W.W., DeWitt, W.S., Radford, C.E., Matsen, F.A., 4th, and Bloom, J.D. (2022). A biophysical model of viral escape from polyclonal antibodies. Virus Evol. *8*, veac110. https://doi.org/10.1093/ve/veac110.

66. Haddox, H.K., Galloway, J.G., Dadonaite, B., Bloom, J.D., Matsen, F.A., and DeWitt, W.S. (2023). Jointly modeling deep mutational scans identifies shifted mutational effects among SARS-CoV-2 spike homologs. Preprint at bioRxiv. https://doi.org/10.1101/2023.07.31.551037.

67. Meng, E.C., Goddard, T.D., Pettersen, E.F., Couch, G.S., Pearson, Z.J., Morris, J.H., and Ferrin, T.E. (2023). UCSF ChimeraX: Tools for structure building and analysis. Protein Sci. *32*, e4792. https://doi.org/10.1002/pro.4792.

68. Farrell, A.G., Dadonaite, B., Greaney, A.J., Eguia, R., Loes, A.N., Franko, N.M., Logue, J., Carreño, J.M., Abbad, A., Chu, H.Y., et al. (2022). Receptor-Binding Domain (RBD) Antibodies Contribute More to SARS-CoV-2 Neutralization When Target Cells Express High Levels of ACE2. Viruses *14*, 2061. https://doi.org/10.3390/v14092061.

69. Zhu, Z., Bossart, K.N., Bishop, K.A., Crameri, G., Dimitrov, A.S., McEachern, J.A., Feng, Y., Middleton, D., Wang, L.-F., Broder, C.C., et al. (2008). Exceptionally potent cross-reactive neutralization of Nipah and Hendra viruses by a human monoclonal antibody. J. Infect. Dis. *197*, 846–853. https://doi.org/10.1086/528801.

70. Hallgren, J., Tsirigos, K.D., Pedersen, M.D., Armenteros, J.J.A., Marcatili, P., Nielsen, H., Krogh, A., and Winther, O. (2022). DeepTMHMM predicts alpha and beta transmembrane proteins using deep neural networks. Preprint at bioRxiv. https://doi.org/10.1101/2022.04.08.487609.

71. Katoh, K., and Standley, D.M. (2013). MAFFT multiple sequence alignment software version 7: improvements in performance and usability. Mol. Biol. Evol. *30*, 772–780. https://doi.org/10.1093/molbev/mst010.

72. Minh, B.Q., Schmidt, H.A., Chernomor, O., Schrempf, D., Woodhams, M.D., von Haeseler, A., and Lanfear, R. (2020). IQ-TREE 2: New Models and Efficient Methods for Phylogenetic Inference in the Genomic Era. Mol. Biol. Evol. *37*, 1530–1534. https://doi.org/10.1093/molbev/msaa015.

73. Shapovalov, M.V., and Dunbrack, R.L., Jr. (2011). A smoothed backbone-dependent rotamer library for proteins derived from adaptive kernel density estimates and regressions. Structure *19*, 844–858. https://doi.org/10.1016/j.str.2011.03.019.

STAR★METHODS

KEY RESOURCES TABLE

REAGENT or RESOURCE	SOURCE	IDENTIFIER
Antibodies		
m102.4	Genscript	N/A
nAH1.3	David Veesler	N/A
HENV-32	James Crowe	N/A
HENV-26	James Crowe	N/A
HENV-103	James Crowe	N/A
HENV-117	James Crowe	N/A
MonoRab HA tag antibody (109B2)	GenScript	Cat#A01963
The DYKDDDDK Tag Antibody, Mouse	GenScript	Cat#A00187; RRID: AB_1720813
Goat anti-human IgG Fc	ThermoFisher	Cat#A18818
Bacterial and virus strains		
10-beta electrocompetent cells	NEB	Cat#C3020K
Chemicals, peptides, and recombinant proteins		
Puromycin	Sigma	Cat#P8833-25MG
Trypsin EDTA	Fisher	Cat#MT25053CI
DMEM	Fisher	Cat#MT10013CV
F-12K	ATCC	Cat#30-2004
Tetracycline-free fetal bovine serum	Gemini Bio	Cat#100-800
Penicillin-Streptomycin	Fisher	Cat#MT30002CI
L-glutamine	Fisher	Cat#MT25005CI
BioT transfection reagent	Bioland Scientific	Cat#B01-02
Soluble Pteropus alecto monomeric EFNB2	David Veesler	N/A
Soluble Pteropus alecto dimeric EFNB2	David Veesler	N/A
Soluble Pteropus alecto monomeric EFNB3	David Veesler	N/A
Soluble Pteropus alecto dimeric EFNB3	David Veesler	N/A
EphB3-Fc	R&D Systems	Cat#5667-B3-050
Critical commercial assays		
QIAprep Spin Miniprep Kit	Qiagen	Cat#27106X4
AMPure XP Reagent	Beckman Coulter	Cat#A63880
Bright-Glo Luciferase Assay System	Promega	Cat#E2610
Qubit 1x dsDNA High Sensitivity and Broad Range Assay Kits	Fisher	Cat#Q33231
Lenti-X Concentrator	Takara	Cat#631232
NEBuilder HiFi DNA Assembly Kit	NEB	Cat#E2621
Deposited data		
BioProject for the Nipah RBP data	This paper	NCBI SRA: BioProject PRJNA1194132
Data generated by dms-vep-pipeline-3 for Nipah RBP DMS	This paper	https://github.com/dms-vep/Nipah_Malaysia_RBP_DMS
Experimental models: Cell lines		
Human Embryonic Kidney cells (HEK-293T)	ATCC	CRL-3216
Human Embryonic Kidney cells expressing rtTA (HEK-293T-rtTA)	Dadonaite et al.[33]	N/A
Chinese Hamster Cells (CHO pgsA-745 cells)	ATCC	CRL-2242

(*Continued on next page*)

Continued

REAGENT or RESOURCE	SOURCE	IDENTIFIER
Chinese Hamster Cells expressing Pteropus alecto EFNB2 (CHO-bEFNB2)	This paper	N/A
Chinese Hamster Cells expressing Pteropus alecto EFNB3 (CHO-bEFNB3)	This paper	N/A
Oligonucleotides		
Primers for plasmid cloning and amplification of viral templates via PCR	IDT	Sequences at https://github.com/dms-vep/Nipah_Malaysia_RBP_DMS/blob/master/data/custom_analyses_data/paper_supplementary_data/primer_sequences.csv
Recombinant DNA		
Expression plasmid encoding VSV-G	Dadonaite et al.[33]	Sequence at https://github.com/dms-vep/Nipah_Malaysia_RBP_DMS/blob/master/data/custom_analyses_data/paper_supplementary_data/plasmid_maps/29_HDM_VSV_G.gb
Expression plasmid encoding Nipah Malaysia RBP with cytoplasmic tail deletion	This paper	Sequence at https://github.com/dms-vep/Nipah_Malaysia_RBP_DMS/blob/master/data/custom_analyses_data/paper_supplementary_data/plasmid_maps/3336_HDM_Nipah_RBP_CTdel33.gb
Expression plasmid encoding Nipah Malaysia Fusion protein with cytoplasmic tail deletion	This paper	Sequence at https://github.com/dms-vep/Nipah_Malaysia_RBP_DMS/blob/master/data/custom_analyses_data/paper_supplementary_data/plasmid_maps/3263_HDM_Nipah_F_CTdel22.gb
HDM-Hgpm2	BEI	NR-52517
pRC-CMV-Rev1b	BEI	NR-52519
HDM-tat1b	BEI	NR-52518
Nipah RBP encoding lentivirus backbone	This paper	Sequence at https://github.com/dms-vep/Nipah_Malaysia_RBP_DMS/blob/master/data/custom_analyses_data/paper_supplementary_data/plasmid_maps/3274_pH2rU3_ForInd_Pur_Nipah_RBP_CTdel33.gb
Lentiviral backbone encoding Luc2 and ZsGreen	BEI	NR-52516
Lentiviral backbone encoding Pteropus alecto EFNB2	This paper	Sequence at https://github.com/dms-vep/Nipah_Malaysia_RBP_DMS/blob/master/data/custom_analyses_data/paper_supplementary_data/plasmid_maps/3949_pHAGE2_EF1A_BatEphrinB2_T2A_mCherry_CMV_PuroR_vlow.gb
Lentiviral backbone encoding Pteropus Alecto EFNB3	This paper	Sequence at https://github.com/dms-vep/Nipah_Malaysia_RBP_DMS/blob/master/data/custom_analyses_data/paper_supplementary_data/plasmid_maps/3694_pHAGE2_EF1A_IRES_mCherry_Pteropus_alecto_EFNB3_HA_tag_Extracellular.gb
Software and algorithms		
vep-dms-pipeline-3 v3.5.4	N/A	https://github.com/dms-vep/dms-vep-pipeline-3
alignparse v0.6.2	Crawford and Bloom[63]	https://github.com/jbloomlab/alignparse
neutcurve v0.5.7	Loes et al.[64]	https://github.com/jbloomlab/neutcurve
dms_variants v1.4.3	N/A	https://github.com/jbloomlab/dms_variants
polyclonal v6.9	Yu et al.[65]	https://github.com/jbloomlab/polyclonal

(*Continued on next page*)

Continued

REAGENT or RESOURCE	SOURCE	IDENTIFIER
dmslogo v0.7.0	N/A	https://github.com/jbloomlab/dmslogo
multiDMS v0.2.1	Haddox et al.[66]	https://github.com/matsengrp/multidms
ChimeraX v1.6.1	Meng et al.[67]	https://www.cgl.ucsf.edu/chimerax/

METHOD DETAILS

Data availability and interactive plots of results

All code and data are publicly available here (https://github.com/dms-vep/Nipah_Malaysia_RBP_DMS), with a landing page with links to specific Jupyter notebooks used at each step in the analysis (https://dms-vep.org/Nipah_Malaysia_RBP_DMS/). The main analyses were all performed with dms-vep-pipeline-3 (https://github.com/dms-vep/dms-vep-pipeline-3).

Raw data from all DMS experiments are available in the main GitHub repository (https://github.com/dms-vep/Nipah_Malaysia_RBP_DMS), with final filtered.csv files in this directory (https://github.com/dms-vep/Nipah_Malaysia_RBP_DMS/tree/master/results/filtered_data/public_filtered).

To explore the cell entry data, heatmaps are available separately for CHO-bEFNB2 (https://dms-vep.org/Nipah_Malaysia_RBP_DMS/htmls/E2_entry_heatmap.html) and CHO-bEFNB3 (https://dms-vep.org/Nipah_Malaysia_RBP_DMS/htmls/E3_entry_heatmap.html) which provide the data with our recommended filters.

If further exploration of the data is desired, there are also heatmaps which provide greater control of parameter filtering (CHO-bEFNB2 here:https://dms-vep.org/Nipah_Malaysia_RBP_DMS/htmls/CHO_bEFNB2_func_effects.html, CHO-bEFNB3 here: https://dms-vep.org/Nipah_Malaysia_RBP_DMS/htmls/CHO_bEFNB3_func_effects.html).

The key filtering parameters for these plots are described below:

- *minimum times_seen*: The minimum number of times a mutation is detected, averaged across libraries and replicates. Mutations with higher 'times_seen' are more likely to have more accurate measurements of effects.
- *maximum effect_std*: The maximum cutoff for the standard deviation of mutant effects. Mutations with lower standard deviations are more likely to be accurate.
- *minimum n_selections*: The minimum number of independent selections a mutation must be detected.
- *minimum max of effect at site*: Filters sites based on the minimum max effect. Allows the users to only view a subset of sites which have beneficial mutations.

To explore the receptor binding data, interactive heatmaps are available for bEFNB2 (https://dms-vep.org/Nipah_Malaysia_RBP_DMS/htmls/E2_binding_heatmap.html) and bEFNB3 (https://dms-vep.org/Nipah_Malaysia_RBP_DMS/htmls/E3_binding_heatmap.html). These have been pre-filtered based on specific criteria (see methods section *Data filtering*) and represent the easiest way to explore the data. For more control over the heatmaps, including parameter filtering and additional interactivity, pages are available here for bEFNB2 (https://dms-vep.org/Nipah_Malaysia_RBP_DMS/htmls/bEFNB2_monomeric_mut_effect.html) and bEFNB3 (https://dms-vep.org/Nipah_Malaysia_RBP_DMS/htmls/bEFNB3_dimeric_mut_effect.html). Here, users can also use the sliders described previously, along with adjusting the *minimum functional effect*, which controls the minimum cell entry score for a mutant to be shown in the receptor binding heatmap.

To explore the antibody escape data, an interactive heatmap for all antibodies is here (https://dms-vep.org/Nipah_Malaysia_RBP_DMS/htmls/mab_plot_all.html). The data have been pre-filtered and enable easier interpretation, and includes information about antibody contact distance for the antibodies that have structures available. More in-depth heatmaps are available for each antibody separately:

- m102.4 (https://dms-vep.org/Nipah_Malaysia_RBP_DMS/htmls/m102.4_mut_effect.html)
- nAH1.3 (https://dms-vep.org/Nipah_Malaysia_RBP_DMS/htmls/nAH1.3_mut_effect.html)
- HENV-26 (https://dms-vep.org/Nipah_Malaysia_RBP_DMS/htmls/HENV26_mut_effect.html)
- HENV-32 (https://dms-vep.org/Nipah_Malaysia_RBP_DMS/htmls/HENV32_mut_effect.html)
- HENV-103 (https://dms-vep.org/Nipah_Malaysia_RBP_DMS/htmls/HENV103_mut_effect.html)
- HENV-117 (https://dms-vep.org/Nipah_Malaysia_RBP_DMS/htmls/HENV117_mut_effect.html)

These heatmaps give the user further control over the filtering parameters with interactive sliders.

Plasmid maps and primer sequences

Maps for all plasmids used in study are available here (https://github.com/dms-vep/Nipah_Malaysia_RBP_DMS/tree/master/data/custom_analyses_data/paper_supplementary_data/plasmid_maps). Primer sequences are available here (https://github.com/dms-vep/Nipah_Malaysia_RBP_DMS/blob/master/data/custom_analyses_data/paper_supplementary_data/primer_sequences.csv).

Creation of CHO-bEFNB2 and CHO-bEFNB3 target cells

In order to isolate the effects of EFNB2 and EFNB3 on viral entry, we sought to make stable cells that would only express one receptor at a time. In addition, to alleviate biosecurity concerns with identifying human specific adaptations, we made target cells that express the bat orthologs of each receptor, rather than human. Finally, we wanted the expression of bEFNB2 and bEFNB3 in the target cells to be roughly similar to a clonal cell line (293T), as extremely high expression of ephrin could bias the DMS results.[68]

To that end, we used Chinese Hamster Ovary (CHO pgsA-745) cells from ATCC (CRL-2242) because they do not express any ephrins.[11,12] Next, we identified the EFNB2 (GenBank Accession: NP_001277099.1) and EFNB3 (ELK03828.1) amino-acid sequences from a natural host of Henipaviruses (*Pteropus alecto*, the black flying fox) in GenBank. Codon optimized versions of these sequences were synthesized by Twist Biosciences. These sequences were cloned into a lentivirus backbone (see the maps for the plasmids 3949_pHAGE2_EF1A_BatEphrinB2_T2A_mCherry_CMV_PuroR_vlow, 3694_pHAGE2_EF1A_IRES_mCherry_Pteropus_alecto_EFNB3_HA_tag_Extracellular linked in the *Plasmid maps* section of the methods above) under the EF1 alpha promoter. The bEFNB3 construct included an N-terminal extracellular HA tag while the bEFNB2 construct did not. The reason the motifs flanking the bEFNB2 and bEFNB3 sequences are slightly different is because we originally used FLAG and HA tags on both bEFNB2 and bEFNB3, respectively, and attempted to sort cells with different expression levels based on staining with anti-FLAG and anti-HA antibodies. While the bEFNB3 clones had reasonable expression levels as measured by flow cytometry, all of the bEFNB2 clones had very high levels of expression. Therefore, we modified bEFNB2 expression further by introducing a non-ideal 6bp Kozak sequence (AATTTT) before the bEFNB2 start codon.[68] This resulted in isolation of a CHO-bEFNB2 clone that had lower bEFNB2 expression than the previous attempt, which was comparable to ephrin expression in 293T cells and the bEFNB3 clones (Figure 2E). Specific details about stable cell isolation are given below.

To produce lentivirus expressing bEFNB2 or bEFNB3, we transfected 1 ug of backbone with 250 ng of lentiviral helper plasmids (26_HDM_Hgpm227, 27_HDM_tat1b, 28_pRC_CMV_Rev1b, 29_HDM_VSV_G) into 293T cells using the BioT transfection reagent following manufacturers directions. After 48 hours, the supernatant was passed through a 0.45 μm syringe filter (Corning, Cat. No. 431220) and stored at -80°C. The generated lentivirus was then used to infect CHO cells at an MOI between 0.1 and 0.01. Individual bEFNB3 expressing cells were sorted 48 hrs later into individual wells of a 96 well plate on a BD Aria II and gated to include only live, single, mCherry positive cells. bEFNB2 expressing CHO cells were passaged in puromycin (1-5 ug/mL) for 1 week and then stained with EphB3-Fc (5667-B3-050; R&D Systems), a natural ligand of EFNB2/3, followed by secondary staining with a Goat anti-human IgG Fc (ThermoFisher A18818). Individual bEFNB2 expressing cells were then sorted into individual wells of a 96 well plate on a Sony MA900 and gated to include only live, single, mCherry positive cells with EFNB expression (FITC) in the same range of 293T cells. Clones of both cell types were then selected based on additional EphB3 staining to ensure they were expressing correct levels of either bEFNB2 or bEFNB3 and for their ability to support high Nipah pseudotyped lentivirus titers (Figure 2F).

Anti-RBP monoclonal antibodies

m102.4 was synthesized by GenScript based on the original sequence deposited of the antibody.[46,69] HENV-26, HENV-32, HENV-103, HENV-117, and nAH1.3 were produced as previously described.[20,21,31]

Lentivirus backbone for RBP deep mutational scanning

The lentivirus vector we used for the pseudovirus deep mutational scanning has been previously described,[33,34] and is schematized in Figures 1A, 1B. A codon-optimized Nipah RBP sequence based on GenBank accession NC_002728.1 lacking 33 amino acids in the cytoplasmic tail at the N-terminus of the protein was inserted into a pHAGE2 based lentivirus vector where the 3′ LTR had been repaired (plasmid map 3274_pH2rU3_ForInd_Pur_Nipah_RBP_CTdel33). Repair of the 3′ LTR enabled us to rescue viruses from cell-stored pseudovirus libraries, a requirement in our system to make genotype-phenotype linked pseudoviruses. This Nipah RBP cytoplasmic tail deletion is based on previous work showing NiV pseudotyped lentivirus titers are greatly increased when most of the cytoplasmic tail is removed (see also Figure 2B).[35,36] Rescue of lentiviruses with this vector is dependent on co-transfection of four plasmids (see plasmid maps: 26_HDM_Hgpm227, 27_HDM_tat1b, 28_pRC_CMV_Rev1b, and 3263_HDM_Nipah_F_CTdel22 that contained a 22 amino acid deletion in the cytoplasmic tail but was otherwise unmutated). These plasmids express Nipah F, along with the HIV-1 proteins for Gag/Pol, Tat, and Rev, which are necessary to produce infectious pseudovirus. Genes encoding the different HIV-1 proteins are located on different plasmids and codon optimized to limit the possibility of recombination leading to replication competent HIV. Although our Nipah RBP sequence was downstream of a dox inducible TRE3G promoter, tests showed titers were not improved during rescue when dox was included, suggesting a sufficient amount of RBP is produced from Tat transfection alone. Thus, dox was not used during the rescue of pseudovirus libraries.

RBP mutant library design and production

We sought to include all possible missense mutations in the ectodomain of the Nipah RBP. The location of the RBP ectodomain was inferred by computational prediction of transmembrane motifs in the RBP amino-acid sequence by DeepTMHMM.[70] Based on these predictions, the transmembrane domain is located between RBP sites 49-69 (Figure S2C). To generate the library, we ordered a single mutant library from Twist Biosciences where reference sites 71-602 were mutagenized, and every other position from sites 71-234 included a stop codon. The stop codons were included at a subset of sites to serve as a meaningful negative control, but not so many as to put too many inactive RBPs into the variant libraries. The final QC report from Twist indicated a total of 19 mutants had

failed and were not present in the library (https://github.com/dms-vep/Nipah_Malaysia_RBP_DMS/blob/master/data/custom_analyses_data/paper_supplementary_data/twist_QC_report.csv). In order to have biological replicates we made two separate libraries, called LibA and LibB, which were separately barcoded using PCR with a 16 base random barcode. The PCR conditions are as follows. 25 μL of KOD Hot Start Master Mix (ThermoFisher, Cat. No. 71842-4), 1.5 μL of 10 μM each primer (ForInd_AddBC_2, 5'_for_lib_bcing), 5 ng of mutant library template DNA, and 19 μL of water. The thermocycler conditions were:

1. 95°C for 2 min
2. 95°C for 20 seconds,
3. 55.5°C for 20s with ramp rate of -0.5°C/sec,
4. 70°C for 1 minute.
5. Return to step 2 for 9x cycles
6. 12°C hold

The vector was prepared by cutting plasmid 3260_pH2rU3_ForInd_mCherry_T7_CMV_ZsGT2APurR with restriction enzymes XbaI and MluI-HF (NEB, Cat. No. R0145S and R3198S). PCR products and cut vector were run on a 1.5% agarose gel, and bands of the correct size were excised and cleaned up with a NucleoSpin Gel and PCR Clean-up kit (Macherey-Nagel, Cat. No. 740609.5) followed by cleanup with Ampure XP beads (Beckman Coulter, Cat. No. A63881). Barcoded mutant variants were then cloned into the cut vector using the NEBuilder HiFi DNA Assembly Kit (NEB, Cat. No. E2621) with a 1:3 insert to vector molar ratio in a 1 hour reaction. HiFi reactions were purified with Ampure XP beads, and DNA was eluted into molecular grade water. We transformed the purified HiFi reaction into 10-beta electrocompetent cells (NEB, Cat. No. C3020K) with a BioRad MicroPulser Electroporator (Cat. No. 1652100), shocking at 2 kV. Bacteria were then plated on 15 cm LB+amp plates and grown overnight at 37°C. To not bottleneck our library diversity at this stage, we sought to make plasmid libraries with a large number of separate colonies. Total colonies for LibA and LibB were $2x10^6$ and $3x10^6$, respectively. Bacteria colonies were scrapped off the plate and eluted in LB+ampicillin, followed by DNA extraction with a Qiagen HiSpeed Plasmid Maxi Kit (Cat. No. 12662).

Rescue of RBP pseudovirus library from transfection and creation of cell-stored mutant library

In order to perform DMS with lentiviruses, we needed to be able to link the genotype and phenotype of RBP variants contained in the vector and the protein expressed on the surface of each virion (See Figure 1C). Pseudoviruses rescued from transfection will contain a mixed population of RBP proteins on the surface of each virion. Additionally, HIV is pseudodiploid and contains two copies of each RNA genome which necessitates production of pseudoviruses from a single vector sequence in each cell to ensure recombination does not scramble the link between barcodes and specific mutations. Therefore, we used a method (originally described in Dadonaite et al.[33]) to integrate each pseudovirus as a single copy in a cell, which enables us to generate full genotype-phenotype linked pseudovirus libraries.

The specific method is as follows. 1 μg of the RBP mutant library lentiviral backbone, 250 ng of each lentiviral helper plasmid (26_HDM_Hgpm227, 27_HDM_tat1b, 28_pRC_CMV_Rev1b), and 250 ng of VSV-G (29_HDM_VSV_G) were transfected into 293T cells plated on 6-well plates using BioT transfection reagent (Bioland Scientific, Cat. No. B01-02). After 48 hours, the supernatant was filtered through a 0.45 μm syringe filter (Corning, Cat. No. 431220) and stored at -80°C.

The final pseudovirus variant libraries require a specific number of variants to ensure accurate DMS measurements. If too few variants are present in a library, we would either fail to detect certain mutations, or only have variants associated with a small number of barcodes, which limits measurement accuracy. If too many variants are present, we would have difficulty obtaining high enough pseudovirus titers to ensure all variants are measured during the selection conditions. Therefore, we controlled variant library size by bottlenecking the virus produced from transfections above.

Briefly, an aliquot of virus was thawed and used to infect 293T cells to obtain a titer (transcription units per mL, TU/mL) based on percent positive ZsGreen cells by flow cytometry. Next, this virus was used to infect M3 293T-rtTA cells, which are stable clones expressing reverse tetracycline transactivator (rtTA) and have been selected to maximally express virus from individual proviruses as previously described in Dadonaite et al.[33] Cells were infected at 0.5% multiplicity of infection (MOI), to ensure each cell contains at most one integrated provirus. Based on estimates for the number of cells present at infection, along with the MOI, we estimated there were ~60,000 unique variants for each library. The MOI was confirmed by flow cytometry based on the percent of cells that were ZsGreen positive, and cells were subjected to 1 μg/mL puromycin selections for 1 week (changing media, passaging cells, adding fresh puromycin every 48 hours) until only ZsGreen positive cells were observed under a fluorescent microscope. We note that the final number of unique variants present in each library were close to the original 60,000 we estimated above (LibA had 78,450 unique barcodes, LibB had 60,623 variants; Table S1). We ensured the library was not bottlenecked by passaging a minimum of 10 million cells each time. Cells were frozen in the gas phase of liquid nitrogen in aliquots of 10 or 20 million cells / mL.

Rescue of RBP and F expressing pseudoviruses from cell-stored mutant library

Viral selections require a high titer of pseudoviruses to ensure there is no bottlenecking of the library diversity, which would skew the measurements. To get high enough titers, we rescued pseudoviruses from a large number of cells, followed by concentration to obtain the final library that can be used to perform selections. Specific methods are as follows. To rescue virus from our integrated

cell libraries, cells were grown in 5-layer flasks (Corning Falcon 875cm^2 Rectangular Neck Cell Culture Multi-Flask, Cat. No. 353144) in 150 mL of D10 until 70% confluent. For each 5-layer flask, a transfection mix was prepared as follows. For Nipah pseudovirus, 60 μg of each helper plasmid (26_HDM_Hgpm227, 27_HDM_tat1b, 28_pRC_CMV_Rev1b) were combined with 8 μg of plasmid 3263_HDM_Nipah_F_CTdel22, 9.2 mL of sera free DMEM, and 276 μL of BioT transfection reagent. After incubating at room temperature for 15 minutes, the transfection mix was added to the 5-layer flasks. For VSV pseudovirus, the same procedure as above was used except plasmid 29_HDM_VSV_G replaced the 3263_HDM_Nipah_F plasmid. After 40 hours, the supernatant was filtered through a 0.45um SFCA Nalgene 500mL Rapid-Flow filter unit (Cat. No. 09-740-44B). We concentrated the supernatant by adding Lenti-X Concentrator (Takara, Cat. No. 631232) at a ratio of 1:3, incubating at 4°C for 4 hours, followed by spinning for 45 minutes at 1500 rcf at 4°C. The supernatant was discarded, and viral pellets were resuspended in F-12K media. Following concentration, the titer of concentrated library virus was ~1*10^6 TU/mL, and frozen in 1 mL aliquots at -80°C.

Long-read sequencing to link mutations to barcodes

To link RBP variants with barcodes, we sequenced the entire RBP plus a 16-bp random nucleotide barcode at the 5' end using PacBio long-read sequencing (see Figure 1B; protocol originally described in Dadonaite et al[33]). The cell-stored libraries were transfected and viruses were rescued as above, except using 29_HDM_VSV_G in place of 3263_HDM_Nipah_F_CTdel22. 293T cells were then infected with ~5-10x10^6 TU of virus. After 12-16 hours, episomal DNA was extracted (see section *Extraction of lentiviral episomal DNA*). 1st round PCR conditions were done in two separate reactions that add a single nucleotide base (either G or C) at the 5' and 3' end of the full amplicon to identify strand exchange, so those variants can be filtered downstream. 1st round PCR conditions are as follows. 20 μL of KOD enzyme, 10 μL of DNA prepared from miniprep, 1 μL each of BL_PacBio_5pri_G and BL_PacBio_3Pri_C (both at 10uM) or 1 μL each of BL_PacBio_5pri_C and BL_PacBio_3pri_G, and 8 μL of molecular grade water. The thermocycler conditions were:

1. 95°C for 2 min
2. 95°C for 20 seconds
3. 70°C for 1 second
4. 60°C for 10 seconds with a ramp rate of -0.5°C/sec,
5. 70°C for 1 minute.
6. Return to step 2 for 7x cycles
7. 12°C hold

The PCR products of the two separate reactions for each library were pooled and cleaned up with Ampure XP beads at a 0.8:1 bead to DNA ratio. The conditions for the 2nd round PCR are as follows. 25 μL of KOD enzyme, 2 μL of each primer at 10 μM (5'_PB_Rnd2 and 3'_PB_Rnd2), and 21 μL of cleaned round 1 product. The thermocycler conditions were:

1. 95°C for 2 min
2. 95°C for 20 seconds
3. 70°C for 1 second
4. 60°C for 10 seconds with a ramp rate of -0.5°C/sec,
5. 70°C for 1 minute.
6. Return to step 2 for 10x cycles
7. 12°C hold

PCR products were then cleaned with AMPure XP beads at a 0.8:1 ratio, followed by sequencing on a PacBio Sequel IIe.

To analyze the PacBio sequencing data and link barcodes to variants, we used *alignparse* (https://github.com/jbloomlab/alignparse).[63] Sequencing reads were first filtered by error rate (*max_ccs_error_rate* <= *1e-4*, which removed approx. 20% of reads for LibA and B). CCSs that did not contain a barcode (~2% of reads), or that were the result of strand exchange (~<1%), as identified by the information contained within the C or G nucleotides added during PCR, were also filtered. Next, CCSs were aligned to a Nipah RBP vector reference sequence, and consensus sequences were generated that contained at least three CCSs and less than a fraction of 0.2 for minor sub or indel frequencies within each consensus sequence. A barcode-variant lookup table was made based on the these consensus sequences, with an empirical accuracy of 0.8 for LibA and LibB and is available at the link here: (https://github.com/dms-vep/Nipah_Malaysia_RBP_DMS/blob/master/results/variants/codon_variants.csv). Jupyter notebooks are available for the specific PacBio filtering steps (https://dms-vep.org/Nipah_Malaysia_RBP_DMS/notebooks/analyze_pacbio_ccs.html), the building of PacBio consensus sequences (https://dms-vep.org/Nipah_Malaysia_RBP_DMS/notebooks/build_pacbio_consensus.html), and the generation of the barcode-variant tables (https://dms-vep.org/Nipah_Malaysia_RBP_DMS/notebooks/build_codon_variants.html).

Extraction of lentiviral episomal DNA

In order to recover information about which variants entered cells following each selection condition, we needed to be able to sequence the barcode sequence from each infecting pseudovirus. Although it might be possible to sequence integrated provirus following infection, the high amount of gDNA that would be co-extracted from cells poses a difficulty due to PCR efficiency.

Therefore, we used a method (as originally described in Dadonaite et al.[33]) to specifically extract episomal lentiviral DNA following cell entry and reverse transcription but prior to integration, which ensures a higher fraction of extracted DNA is of lentiviral origin, rather than host cell. Prior to integration, episomal lentiviral dsDNA will be present in the nucleus as low molecular weight DNA, which can be selectively extracted from cells using a plasmid DNA extraction kit. The specific details are as follows: $5*10^5$ CHO-bEFNB2 or CHO-bEFNB3 cells were plated in 6-well plates in 2 mL of F-12K media. Pseudoviruses were added (refer to specific sections on each type of selection for more information). For all selection conditions, 12-16 hours after infection, cells were trypsinized and spun down at 300 rcf for 4 minutes. We then extracted episomal DNA using a Qiagen QIAprep Spin Miniprep Kit (Cat. No. 27106), following manufacturer's directions and eluted into 30 μL of Buffer EB.

Illumina barcode sequencing

To amplify lentivirus genome barcodes, we added 22 μL of extracted episomal DNA (described in the section *Extraction of lentiviral episomal DNA*) to a reaction containing 25 μL KOD, and 1.5 μL each of 10 μM Illumina_Rnd1_For and Illumina_Rnd1_Rev primers. The thermocycler conditions were:

1. 95°C for 2 min
2. 95°C for 20 seconds
3. 70°C for 1 second
4. 58°C for 10 seconds with a ramp rate of -0.5°C/sec,
5. 70°C for 20 seconds.
6. Return to step 2 for 27x cycles
7. 12°C hold

First round products were then cleaned with Ampure XP beads at a ratio of 1:1. 2 μL of cleaned 1st round product diluted to 5 ng/μL was then mixed with 25 μL KOD, 19 μL of molecular grade water, and 2 μL each of 10 μM Illumina_Rnd2_Fwd and a unique index contained with the Illumina_Rnd2_Index_Rev primer. Thermocycler conditions were almost identical to the first round, except using 20 total cycles.

DNA concentration was determined with a Qubit 4 Fluorometer (ThermoFisher, Cat. No. Q33238), and PCR products were pooled in equal DNA amounts, followed by running on a 2% Agarose Gel. The correct band size (283bp) was clipped on a blue light gel dock, followed by extraction with a NucleoSpin Gel and PCR Clean-up kit. The final DNA library was then cleaned up with Ampure XP beads at a ratio of 1:1, and the DNA concentration was determined on a Qubit 4. The final library was diluted to 4 nM, and single read sequencing was done with a NextSeq P1 or P2 kit for 50 cycles. To account for sequencing errors and to ensure each variant was sequenced multiple times (to obtain accurate frequency estimates of each barcode), we oversequenced each selection, and recovered ~10-85 million reads total. Thus, each barcode in a selection was sequenced on average 90-600 times, depending on the exact read depth. Details on the number of Illumina reads mapping to each selection, and the average number of reads per barcode are given in this notebook (https://dms-vep.org/Nipah_Malaysia_RBP_DMS/notebooks/analyze_variant_counts.html).

Validations of DMS data using single mutant Nipah pseudoviruses

To validate our DMS measurements, we made single RBP mutant pseudoviruses and compared their entry or neutralization to unmutated Nipah RBP. For RBP entry, we made RBP mutants C162L, F168A, Y389T, P488S, Q492L, Q530F, Q530E, and Q530L. For receptor neutralization validations, we made mutants H333Q, Q492R, V507I, Q530F, S553W, and D555K. For antibody neutralization, we made mutants L184H, P185D, Q450S, D468V, I517K, W519T, and I520T.

Specifically, we introduced single amino-acid mutations using PCR with partially overlapping primers that contained the desired mutations. Primers were designed with the online NEBaseChanger software. For PCR, 10 ng of plasmid 3336_HDM_Nipah_RBP_CTdel33 was added to two reactions containing 25 μL KOD, and 1.5 μL each of 10 μM For_primer and Rev_mutagenesis_primer or Rev_primer, Forward_mutagenesis_primer. The thermocycler conditions were:

1. 95°C for 2 min
2. 95°C for 20 seconds
3. 58°C for 10 seconds
4. 70°C for 30 seconds.
5. Return to step 2 for 24x cycles
6. 12°C hold

Following PCR, the two amplicons were cloned into plasmid 27_HDM_tat1b after cutting with NotI and HindIII, with the NEBuilder Hifi DNA Assembly Kit incubating at 50°C for 1 hour, and transformed into Stellar competent cells (Takara, Cat. No. 636763). For cell entry validation mutants, three separate plasmids were isolated; for receptor binding or antibody neutralization validation only one plasmid was isolated per mutant. All mutants were confirmed by whole plasmid sequencing by Primordium. To make virus, 293T cells were plated on 6-well plates in 2mL of D10 media. 16-24 hours later, 1ug of plasmid 2727_pHAGE6-wtCMV-Luc2-BrCr1-ZsGreen-W-1247, 500ng of 26_HDM_Hgpm2, and 250ng each of 3263_HDM_Nipah_F_CTdel22, and either the unmutated RBP expression

plasmid 3336_HDM_Nipah_RBP_CTdel33, or a mutant expression plasmid. An example of a mutant expression plasmid is 3922_HDM_Nipah_RBPctDel_P185D. After 48 hours, the supernatant was passed through a 0.45 uM filter.

For cell entry validations, three separate plasmid preps of each RBP variant were used to generate three separate virus stocks. Viruses were added to either CHO-bEFNB2 or CHO-bEFNB3 cells plated a day earlier in poly-L-lysine coated, black walled, 96-well plates (Greiner, Cat. No. 655930). For each plasmid prep, two replicates were run on the same plate at three different dilutions to ensure we were in the correct dynamic range. Each plate also contained a cell only and virus only condition to correct for any background luciferase signal. 48 hours later, 170 μL of supernatant was removed from each well, followed by the addition of 30 μL of Bright-Glo Luciferase Assay System (Promega, E2610). Luciferase values were immediately read on a Tecan Infinite M1000 plate reader. The relative light units (RLU) per μL were calculated separately for each mutant. The data for validation assays for CHO-bEFNB2 cells are here (https://github.com/dms-vep/Nipah_Malaysia_RBP_DMS/blob/master/data/custom_analyses_data/experimental_data/functional_validations_EFNB2.csv) and for CHO-bEFNB3 cells here (https://github.com/dms-vep/Nipah_Malaysia_RBP_DMS/blob/master/data/custom_analyses_data/experimental_data/functional_validations_EFNB3.csv).

To validate DMS measurements for antibody and receptor neutralization, the same strategy was used as above, except luciferase expressing pseudoviruses were incubated with antibody or soluble receptor for one hour prior to adding to cells. For antibody validations, we used a starting concentration of 10 ug/mL of nAH1.3 and did eight three-fold dilutions. A no-antibody or no-receptor control were run in duplicate. Fraction infectivity was calculated by subtracting background readings and comparing the amount of signal in each well with the average luciferase reading from two wells with no antibody or no receptor. Fraction infectivity values for the antibody validations are here (https://github.com/dms-vep/Nipah_Malaysia_RBP_DMS/blob/master/data/custom_analyses_data/experimental_data/nAH1_3_mab_validation_neuts.csv), and for receptor validations here (https://github.com/dms-vep/Nipah_Malaysia_RBP_DMS/blob/master/data/custom_analyses_data/experimental_data/binding_single_mutant_validations.csv). IC_{50} values were estimated by fitting neutralization curves using the package *neutcurve* (https://github.com/jbloomlab/neutcurve).[64]

Production of a VSV-neutralization standard virus

To estimate absolute neutralization across different conditions, we used pseudoviruses expressing VSV-G that were not neutralized by ephrin receptors or anti-RBP antibodies, and spiked them into the receptor binding and antibody selections to represent ~1% of reads in the no-antibody or no-receptor control selections (see below). The VSV-G neutralization standard viruses were produced as described in Dadonaite et al[33] Briefly, a sequence encoding mCherry that was associated with eight known 16bp barcodes was cloned into a lentiviral vector (plasmid 3260_pH2rU3_ForInd_mCherry_T7_CMV_ZsGT2APurR). These viruses were rescued by transfection with plasmid expressing VSV-G and the other helper plasmids in 293T cells, followed by transduction of M3 293T-rtTA cells at low MOI, to ensure no more than one vector was integrated per cell. Pseudoviruses were then rescued as described above, and titered on 293T cells to be able to spike in a known amount relative to the RBP/F pseudovirus libraries.

Selections to determine effects of mutations on cell entry

To determine the effects of mutations on cell entry, we used a strategy where barcode frequencies between VSV-G pseudotyped lentiviral mutants are compared with barcodes for pseudoviruses with Nipah RBP and unmutated F (see also Figure S1A). Because VSV-G efficiently infects cells irrespective of which RBP variant is on the virion surface, it is used as a 'control' for determining the baseline composition of the mutant library. RBP mutants will have variable ability to enter cells and can thus be compared with the baseline composition.

Specifically, we plated $7.5*10^5$ CHO-bEFNB2 or CHO-bEFNB3 in 2mL of F12-K media in individual wells of a 6-well plate. The next day, ~$5*10^6$ VSV-G pseudotyped viruses were added to cells, or ~$1*10^6$ Nipah RBP/F pseudoviruses. 12-16 hours later, episomal DNA was extracted from cells (see section *Extraction of lentiviral episomal DNA*), followed by Illumina sequencing (see section *Illumina barcode sequencing*).

We performed at least two independent cell entry selections from each library, although in some cases we included more to improve confidence of DMS measurements. For estimating cell entry in CHO-bEFNB2 cells, we performed six LibA and two LibB selections independently. For estimating cell entry in CHO-bEFNB3 cells, we performed three LibA and four LibB selections.

To analyze the Illumina sequencing data, we used the package *dms_variants* (https://github.com/jbloomlab/dms_variants) to parse the read data and estimate functional scores associated with each variant. Barcodes were aligned to the codon-variant table previously produced from PacBio long-read sequencing.

Raw barcode counts were converted to functional scores as previously described in Dadonaite et al.[33] Briefly, functional scores were calculated using enrichment ratios: $\log_2([n^v_{post} / n^{wt}_{post}]/[n^v_{pre}/n^{wt}_{pre}])$ where n^v_{post} is the count of variant *v* in the Nipah RBP pseudotyped infection, n^v_{pre} is the count of variant *v* in the VSV-G pseudotyped preselection condition, n^{wt}_{pre} is the count of unmutated variants in the VSV-G pseudotyped preselection condition, and n^{wt}_{post} is the count of unmutated variants in the Nipah RBP pseudotyped infection. The dynamic range of our assay is such that we can only reliably measure cell entry down to -4 (corresponding to 16-fold decrease in cell entry relative to unmutated), which is typically the value observed for stop codon mutations. Thus, scores between -4 and 0.5 indicate changes in cell entry ranging from a 16-fold decrease to a 1.4-fold increase relative to the unmutated strain.

Raw barcode counts can be found here (https://github.com/dms-vep/Nipah_Malaysia_RBP_DMS/tree/master/results/barcode_counts). Because our libraries contained some multi-mutants, we deconvolved the effects of individual mutations on entry with a

global epistasis model[40] implemented in the *multidms* package (https://github.com/matsengrp/multidms). The final entry score we report is taken from the average effect across replicates and libraries.

Selections to determine effects of mutations on receptor binding

To determine the effects of mutations on receptor binding, we used a strategy where pseudoviruses were incubated with varying amounts of soluble receptor, followed by cell infection to recover barcode frequencies for the different conditions (see Figure S1B). The underlying reasoning is that pseudovirus neutralization by soluble receptors should be proportional to its binding. Mutations which increase receptor binding will be neutralized at a lower concentration than unmutated, while mutations which decrease binding will be neutralized at a higher concentration.

Specifically, we plated either $7.5*10^5$ CHO-bEFNB2 or CHO-bEFNB3 in 2mL of F-12K media in individual wells of a 6-well plate. The next day, the mutant pseudovirus library was mixed with 1% of a VSV-G pseudovirus 'neutralization standard' which contains eight different known barcodes (see section *Production of a VSV-neutralization standard virus*). Because VSV-G is not neutralized by soluble bEFNB2 or bEFNB3, its proportion of reads in each condition will vary depending on neutralization of RBP pseudovirus, which allows us to standardize reads across conditions. Next, $\sim 1*10^6$ TU of Nipah RBP/F pseudoviruses were used to either infect cells (control condition) or incubated with varying amounts of soluble monomeric bEFNB2 or dimeric bEFNB3 for one hour. Based on previously determined IC_{50} ranges (Figure 5A) of each soluble receptor, we sought to use concentrations spanning an IC_5 to IC_{95}. Following incubation, pseudoviruses were added to cells (viruses from monomeric bEFNB2 selections infected CHO-bEFNB2 cells, viruses from dimeric bEFNB3 selections infected CHO-bEFNB3 cells). 12–16 hours later, DNA was extracted (see section *Extraction of lentiviral episomal DNA*), followed by Illumina sequencing (see section *Illumina barcode sequencing*).

To analyze the sequencing data, we parsed the Illumina reads as in the previous section. Next, we calculated the binding scores as the $\log_2$ transformed values of: $(F * [n^v_{post} * N_{pre}] / [n^v_{pre} * N_{post}])$, where F is the overall fraction of the library that escapes neutralization, which is derived experimentally from the neutralization standard 'spike-in.' n^v_{post} and n^v_{pre} are the counts of variant *v* in the receptor and no-receptor controls, respectively. N_{pre} and N_{post} are the summed counts of all variants in the receptor and no-receptor controls, respectively. The raw binding scores for each variant can be found here (https://github.com/dms-vep/Nipah_Malaysia_RBP_DMS/tree/master/results/receptor_affinity/by_selection). Next, we fit neutralization curves for each selection to estimate the effects of mutations on receptor neutralization as implemented in the package *polyclonal* (https://jbloomlab.github.io/polyclonal/).[65] At a minimum, we did at least one selection with LibA and LibB, and used the mean effects between these independent replicates in all analyses.

Selections to determine effects of mutations on antibody neutralization

To determine the effect of RBP mutations on antibody neutralization, we used the same general strategy as the receptor selections, except substituting antibodies in place of the soluble receptor proteins. All antibody selections were followed by infection of CHO-bEFNB3 cells. Based on previous IC_{50} values for each antibody (Figure S6A; Table S5), pseudoviruses were incubated with antibody concentrations corresponding to IC_{50}, IC_{90}, and IC_{99}. Neutralization curves were fit as in the previous section. The raw escape scores for each variant can be found here (https://github.com/dms-vep/Nipah_Malaysia_RBP_DMS/tree/master/results/antibody_escape/by_selection). At a minimum, we did at least one selection with LibA, and one with LibB, and used the mean effects between these independent replicates in all analyses.

Data filtering

Raw data were filtered to produce all heatmaps and figures. Briefly, we required mutations to be present in multiple barcodes (*times_seen* > *2*). We also filtered out mutations with a high standard deviation between replicates (*max_std*). Finally, we required mutations to be observed in the majority of individual selections (*frac_models* > *0.5*). These steps remove mutations that have a low number of observations, with high standard deviation between selections, or which were only observed in a subset of individual selections. Notebook for filtering data is here (https://dms-vep.org/Nipah_Malaysia_RBP_DMS/notebooks/filter_data.html), and contains more information about the specific parameters that were used.

Validation of RBP binding measurements by biolayer interferometry

Biolayer interferometry (BLI) was performed on an Octet Red96 (Sartorius) and the Octet Data acquisition. Dimeric *P. alecto* Ephrin B2-hFc was diluted to 10 μg/mL and B3-hFc was diluted to 5 μg/mL in 10x Octet kinetics buffer (Sartorius). Ephrins were then loaded onto hydrated anti-Human-Fc capture (AHC) biosensors to a 1nm shift, equilibrated in 10x Octet kinetics buffer for 60 seconds, and dipped into monomeric RBP head at 11, 3.7, 1.23, and 0.41 nM for EFNB2 and at 900, 300, 100, and 33 nM for EFNB3. The association phase was run for 300s. Dissociation was observed by dipping biosensors in a 10x Octet kinetics buffer for 300s. BLI measurement was performed at 30°C and shaking at 1,000 rpm. Association phases were aligned to 0 seconds and 0 shift in Octet Data Analysis HT software and the processed results were exported. For RBP binding to EFNB2, data were globally fit using a 1:1 binding model using the Octet Data Analysis HT software to obtain equilibrium dissociation constants (K_D). For RBP binding to EFNB3, we used area under the curve to estimate the binding magnitudes due to fast on- and off-rates, limited concentration of EFBN3 relative to the low binding affinity and signal reaching negative values after dissociation for some concentrations.

Nipah virus RBP recombinant production

The wildtype Nipah virus RBP head domain construct contains a Mu phosphatase signal peptide followed by a 6x Histidine tag, a GSGGGS linker and residues 176-602 of the Nipah virus RBP (Genbank ID NP_112027.1) cloned in the pOPING expression vector. The Nipah virus RBP V244W, L305W, Q388P, Q492L, V507I, Q530F, S553W, D555Y, Q559R, and I588V mutants were synthesized and subcloned in the pTwist CMV expression vector using the same construct design as for the wildtype one. Nipah RBP head domains were expressed in Expi293 cells (Thermo) maintained at 37°C and 8% CO_2 with constant shaking. Cells were transfected using Expifectamine293 transfection kit (Thermo) following the manufacturer's protocol. Four days after transfection, Expi293 cell supernatant was clarified by centrifugation at 4,121 x *g* for 30 minutes, and supplemented with 100mM Tris pH 8.0, 300 mM NaCl. Supernatant was then bound to 1 mL of Ni Excel resin (Cytiva) previously equilibrated in 100mM Tris pH 8.0, 300 mM NaCl. Nickel resins were washed with 30 mL of 100mM Tris pH 8.0, 300 mM NaCl, and 20 mM imidazole. Protein was eluted using 100mM Tris pH 8.0, 300 mM NaCl, and 250 mM imidazole prior to being buffer exchanged to 50 mM Tris-HCl pH 7.4, 150 mM NaCl using a centrifugal filter device with a MWCO of 30 kDa. Purified proteins were then stored at 4°C until use. Proteins were run over a Superdex200 increase 10/300 size-exclusion column (Cytiva) equilibrated in 50 mM Tris pH 7.4, and 150 mM NaCl. Fractions containing monodisperse protein were then used for biolayer interferometry.

Monomeric *Pteropus alecto* Ephrin-B2 and -B3 purification

The monomeric *P. alecto* EFNB2 and EFNB3 constructs were codon-optimized for a mammalian cell expression system, synthesized, and cloned into a pTwist CMV vector by Twist Bioscience. These constructs include residues 28 to 224 for *P. alecto* EFNB2 (GenBank accession no. NP_001277099), and residues 29 to 226 for P. alecto EFNB3 (GenBank accession no. NP_001277094), followed by Factor Xa protease site (IEGR), a linker (GSGGGS) and StrepII tag (WSHPQFEK). MPMGSLQPLATLYLLGMLVASVLA was used as the signal peptide for both constructs.

The monomeric *P. alecto* EFNB2 and EFNB3 were expressed in Expi293F cells by transient transfection using the ExpiFectamine 293 Transfection Kit (Thermo Fisher) according to the manufacturer's protocols. After 7 d in a humidified shaking incubator maintained at 37 °C and 8% CO2, the transfected cells were harvested and cleared of cellular debris by centrifugation for 10 min at 1,000 × g followed by centrifugation for 30 min at 10,000 × g. The supernatants were then subjected to affinity chromatography. The monomeric P. alecto EFNB2 and EFNB3 were purified from clarified supernatants using a 1-mL StrepTrap HP column (Cytiva), buffer- exchanged, concentrated, and flash-frozen in TBS (pH 8.0, 25 mM Tris, 150 mM NaCl). All columns were equilibrated in TBS (pH 8.0, 25 mM Tris, 150 mM NaCl). The wash buffer used for all columns was TBS. The elution buffer was TBS with 2.5 mM desthiobiotin.

Pteropus alecto Ephrin B2-hFc and B3-hFc production

The *Pteropus alecto* bEFNB2 and bEFNB3- hFc constructs contain an N-terminal MPMGSLQPLATLYLLGMLVASVLA signal peptide followed by residues 28-224 of bEFNB2 or residues 29 to 226 of bEFNB3, a factor Xa cleavage site followed by a human IgG1 Fc fragment cloned in the pTwist CMV expression vector.

Dimeric *P. alecto* Ephrin B2-hFc and B3-hFc were expressed in Expi293 cells (Thermo) at 37°C and 8% CO_2. Cells were transfected using Expifectamine293 transfection kit (Thermo) following the manufacturer's protocol. Four days after transfection, Expi293 cell supernatant was clarified by centrifugation at 4,121 x *g* for 30 minutes, supplemented with 20 mM phosphate pH 8.0, 100 mM NaCl or 50 mM Tris pH 7.4, and 150mM NaCl. Supernatant was then bound to 1mL HiTrap Protein A column (Cytiva) or MabSelect Affinity resin (Cytiva) previously equilibrated in 20 mM phosphate pH 8.0, and 100 mM NaCl or 50 mM Tris pH 7.4, and 150mM NaCl. Columns were washed with 30 mL of 20 mM phosphate pH 8.0, 100 mM NaCl or 50 mM Tris pH 7.4, and 150mM NaCl. Proteins were eluted using 8 mL of 100 mM citric acid pH 3.0, and 100mM NaCl directly into 2 mL of 1M Tris pH 9.0. Proteins were concentrated using a centrifugal filter device with a MWCO of 30 kDa and run over a Superdex200 increase 10/300 size-exclusion column (Cytiva) equilibrated in 50 mM Tris pH 8.0 or pH 7.4, and 150mM NaCl. Fractions containing monodisperse dimeric protein were stored at 4°C or flash frozen and stored at -80°C until use.

Logo plots

To make logo plots visualizing antibody escape (i.e. Figure 7A), we used the *dmslogo* package (https://github.com/jbloomlab/dmslogo). To select a subset of sites for visualization, we required mutations to have a max escape score within at least 50% of the max escape score for that antibody, or a summed escape score within at least 75% of the max summed escape site for that antibody.

Structural analyses

UCSF ChimeraX v1.6.1[67] was used for all structural analyses and figures. PDB accession IDs for specific structures are given in each figure legend. In some cases, superimposition of structures was required (ex. Figures 2A and S6B), which was done using the *matchmaker* method implemented in ChimeraX using default parameters. To map mutational effects onto the structure, we calculated the site-averaged effects using this notebook (https://dms-vep.org/Nipah_Malaysia_RBP_DMS/notebooks/mapping_site_level.html), which were converted to a.defattr file format required by ChimeraX. Sites were colored using the *color byattr* command function in ChimeraX with the appropriate color scale. To estimate atomic distances between Nipah RBP residues and receptors or

antibodies, we used this notebook (https://dms-vep.org/Nipah_Malaysia_RBP_DMS/notebooks/receptor_distance.html). Receptor and antibody contact sites were calculated by finding all RBP residues within 4 angstroms.

Sequence analysis

To obtain evolution and diversity information regarding Nipah viruses (for example Figures 2A, 7C), we downloaded all publicly available Nipah whole-genome nucleotide sequences from GenBank (as of January 3-2024; GenBank accessions found here https://github.com/dms-vep/Nipah_Malaysia_RBP_DMS/blob/master/data/custom_analyses_data/alignments/phylo/nipah_whole_genome_genbank_accession_ids.txt). Sequences were aligned with MAFFT v7.520,[71] and a maximum-likelihood phylogenetic tree was inferred with IQ-Tree v2.2.2.6[72] with the TIM2 substitution model. The phylogeny was then visualized using the package *baltic 0.2.2* (https://github.com/evogytis/baltic) implemented in this notebook (https://dms-vep.org/Nipah_Malaysia_RBP_DMS/notebooks/make_nipah_phylogeny_baltic.html).

To find all Nipah RBP amino-acid mutations in these sequences, we trimmed the whole-genome sequences to just RBP and translated them to amino-acid sequences in Geneious Prime 2023.0.4. Alignment can be found here (https://github.com/dms-vep/Nipah_Malaysia_RBP_DMS/blob/master/data/custom_analyses_data/alignments/Nipah_RBP_AA_align.fasta). All amino-acid mutations relative to the unmutated reference sequence were found using this notebook (https://dms-vep.org/Nipah_Malaysia_RBP_DMS/notebooks/henipavirus_conservation.html).

We downloaded publicly available Hendra sequences from GenBank (as of 11/17/24), aligned them as described above, and calculated all amino-acid changes relative to the Nipah virus RBP parental strain. The alignment is located here: (https://github.com/dms-vep/Nipah_Malaysia_RBP_DMS/blob/master/data/custom_analyses_data/alignments/hendra_G_AA_aligned.fasta).

To make an amino-acid alignment of human and bat (*Pteropus alecto*) EFNB2 and EFNB3 sequences, we downloaded reference sequences from GenBank and aligned them using MAFFT v7.520. Amino-acid alignment can be found here (https://github.com/dms-vep/Nipah_Malaysia_RBP_DMS/blob/master/data/custom_analyses_data/alignments/ephrin_E2_E3_sequences.fasta).

Figures

To make publication quality images, figures were generated with Vega-Altair v5.1.2 (https://altair-viz.github.io/) or Prism v9.4.1. Font sizes and figure arrangements were adjusted in Adobe Illustrator v27.0.

Supplemental figures

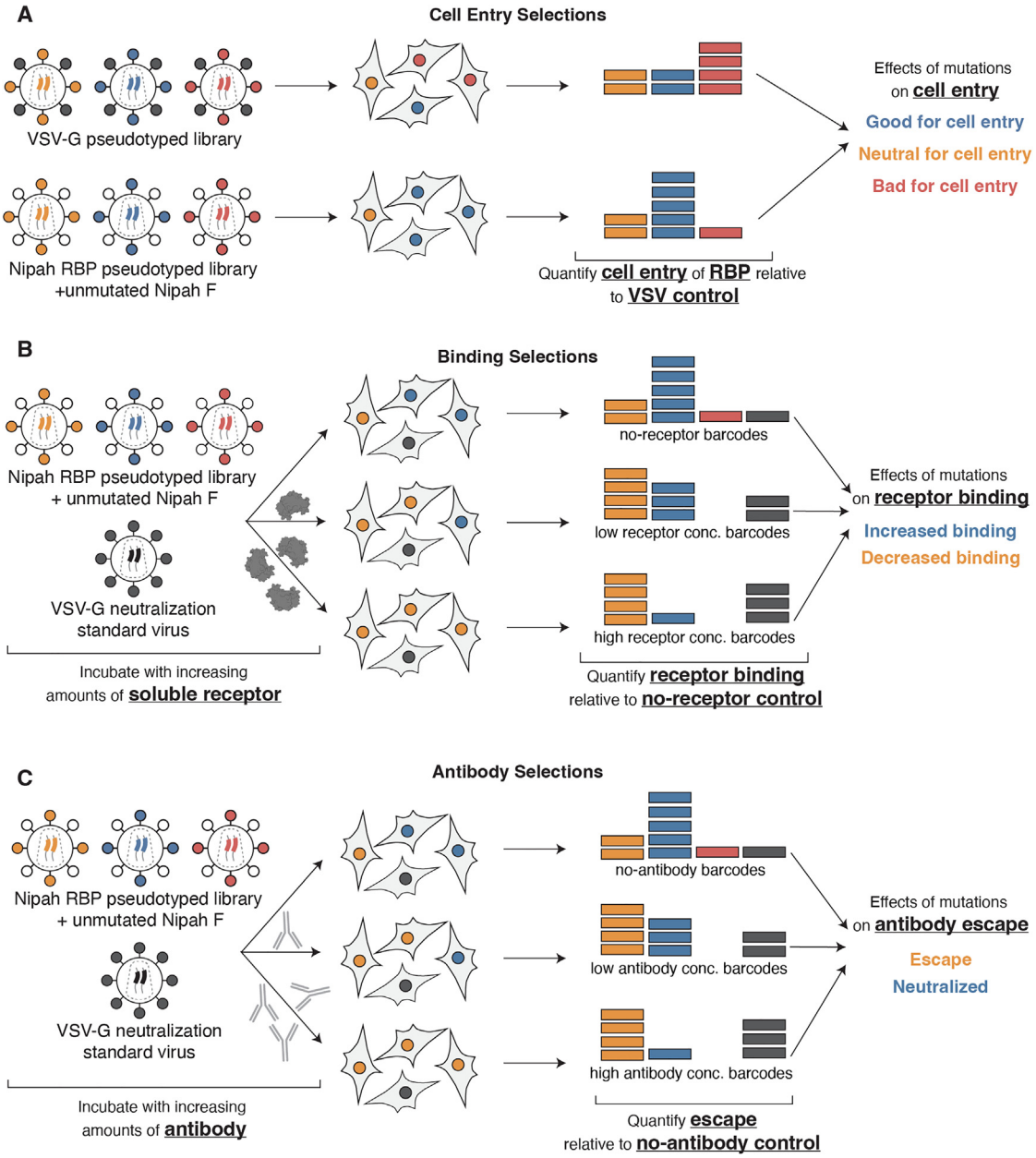

Figure S1. Graphical overview of DMS selections for measuring cell entry, receptor binding, and antibody escape, related to STAR Methods and Figure 1

(A) Cell entry overview. Pseudoviruses with either Nipah RBP + VSV-G (control condition) or Nipah RBP + unmutated Nipah F are used to infect target cells (CHO-bEFNB2 or CHO-bEFNB3). Pseudoviruses with VSV-G on the surface will efficiently infect cells regardless of which RBP variant is expressed on the surface of the virion. 12 h after infection, unintegrated viral DNA is extracted, and barcodes within each lentivirus vector are amplified with PCR and sequenced with Illumina. Reads from the VSV-G control conditions are used to quantify cell entry relative to the Nipah RBP + unmutated F infection condition.

(B) Receptor-binding overview. This approach is based on the fact that inhibition of infection by soluble receptor is proportional to receptor-binding affinity. Pseudovirus libraries with Nipah RBP + unmutated F are mixed with ~1% neutralization "standard" pseudovirus expressing only VSV-G and containing defined barcodes in its genome. Libraries are used to either infect cells with nothing added (the no soluble receptor control) or they are first incubated with soluble receptor at increasing concentrations prior to cell infection. The barcode extraction and sequencing are the same as in (A). Counts from the neutralization

(legend continued on next page)

standard are used to normalize read counts across conditions, followed by quantification of receptor binding by comparing barcode frequencies in the receptor incubation conditions compared with the no receptor control. Mutants that decrease binding to soluble receptor will increase in relative frequency due to decreased neutralization by the receptor. Mutants that increase binding to the receptor will decrease in relative frequency due to being neutralized more.
(C) Antibody selection overview. A neutralization standard is included for antibody selections, similar to the receptor-binding selections. A control condition is also included (the no antibody control), and other conditions use pseudovirus incubated with increasing concentrations of antibody. The barcode extraction and sequencing steps are similar to (A) and (B). Mutants that increase in relative frequency in the presence of neutralizing antibodies are escape mutations.

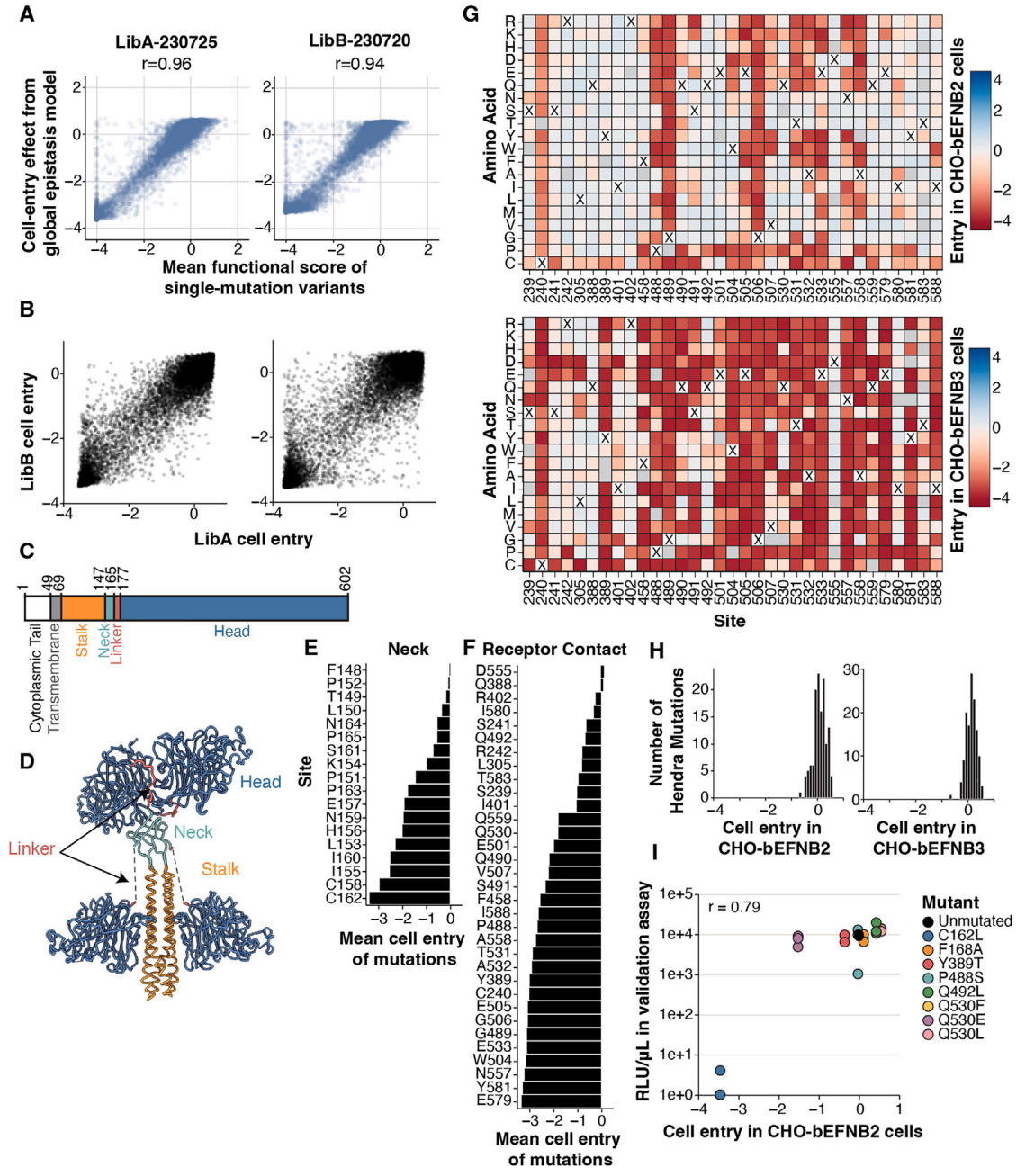

Figure S2. Library correlation statistics, Nipah RBP protein domains, and additional information on effect of mutations on cell entry, related to Figures 3 and 4

(A) Correlations between the effects of mutations as deconvolved by fitting a global epistasis model to all RBP variants versus averaging the measurements for variants with single mutations only. One representative selection in CHO-bEFNB3 cells is shown, with the Pearson correlation coefficient (r) value above. Global epistasis fitting does not dramatically alter the estimated functional effects of mutations.

(B) Correlations between effects of RBP mutations on cell entry in CHO-bEFBN2 or CHO-bEFNB3 cells measured using the two independent RBP pseudovirus libraries (LibA and LibB). For CHO-bEFNB2 cells, we conducted six independent functional selections using LibA and two using LibB. For CHO-bEFNB3 cells, three functional selections were carried out with LibA and four with LibB. For each library, the value plotted here is the mean measurement for each mutation across the different selections with that library. We only show measurements for mutations present in at least two barcoded RBP variants. The Pearson correlation coefficients (r) were 0.92 for both target cell types.

(C and D) Major regions of Nipah RBP. A four-helix bundle (stalk) connects to the transmembrane domain that anchors the RBP in the viral membrane. The neck is a β sandwich that has multiple disulfide bonds and is involved in F-triggering. A flexible linker connects the neck with the globular heads. Two of the heads are arranged above the neck (distal), while two are arranged along the stalk toward the viral membrane (proximal). Note the linker region for the proximal heads was

(legend continued on next page)

not resolved in structure and is indicated with dotted lines. (C) Numbering and location of wild-type RBP domains. (D) RBP tetramer colored by domain (PDB: 7TXZ and 7TY0).

(E and F) Ranked site-averaged effects of mutations on cell entry in CHO-bEFNB3 cells in the neck (E) and receptor contact residues (F), ordered from least constrained (top) to most (bottom). Most mutations at site 555 are tolerated as EFNB2/3 interacts with the backbone and not the side chain. E533 is a key contributor to the receptor-contact interface and forms two salt bridges with K60 and K116.

(G) Effects of RBP mutations on entry in CHO-bEFNB2 and CHO-bEFNB3 at receptor-contact sites. Entry scores for mutations in CHO-bEFNB2 cells are shown on top, and CHO-bEFNB3 is on the bottom. For each mutation, the entry score reflects the cell entry efficiency of a pseudovirus with that RBP mutation relative to the unmutated RBP (log_2 scale). Negative values (red) indicate impaired entry, zero (white) indicates no effect, and positive values (blue) indicate improved entry. The unmutated amino acid in the Malaysia strain RBP at each site is indicated with a "X." An interactive version of this figure is available here (https://dms-vep.org/Nipah_Malaysia_RBP_DMS/htmls/combined_entry_binding_contact_heatmaps.html).

(H) DMS-measured effects of mutations observed in Hendra virus relative to Nipah Malaysia RBP. Hendra virus mutations were largely tolerated in the parental Nipah Malaysia strain used for DMS. To obtain a list of mutations, all Hendra virus sequences were downloaded (from GenBank on 11/17/24) and aligned with the Nipah Malaysia RBP reference strain. Only mutations present in at least two Hendra virus sequences relative to the parental Nipah Malaysia RBP sequence were included.

(I) Validations of DMS measurements of mutational effects on cell entry in CHO-bEFNB2 cells with single-mutant pseudoviruses compared with unmutated. The data shown here are similar to that in Figure 4I, except validations were performed with CHO-bEFNB2 rather than CHO-bEFNB3 cells.

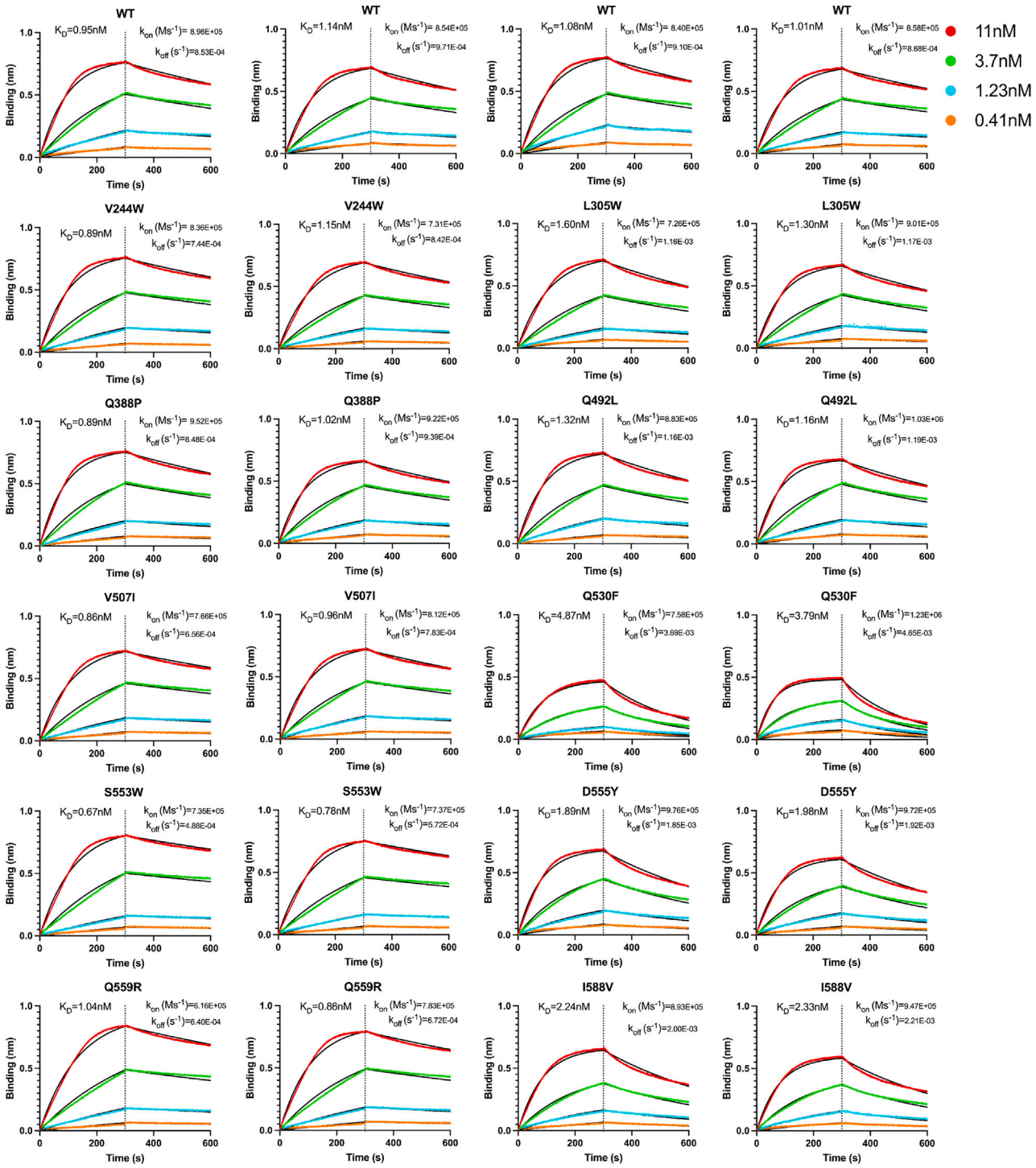

Figure S3. BLI binding of NiV RBP heads to bEFNB2-hFc, related to Figure 5

Data from four replicates of the wild-type (unmutated) RBP and two replicates of each selected mutation are shown for binding to dimeric bEFNB2-hFc immobilized on anti-Human-Fc capture (AHC) biosensors. The K_D, k_{on}, and k_{off} estimated using a 1:1 binding model and global fitting are shown above each plot, and values with standard errors of measurements are reported in Table S2.

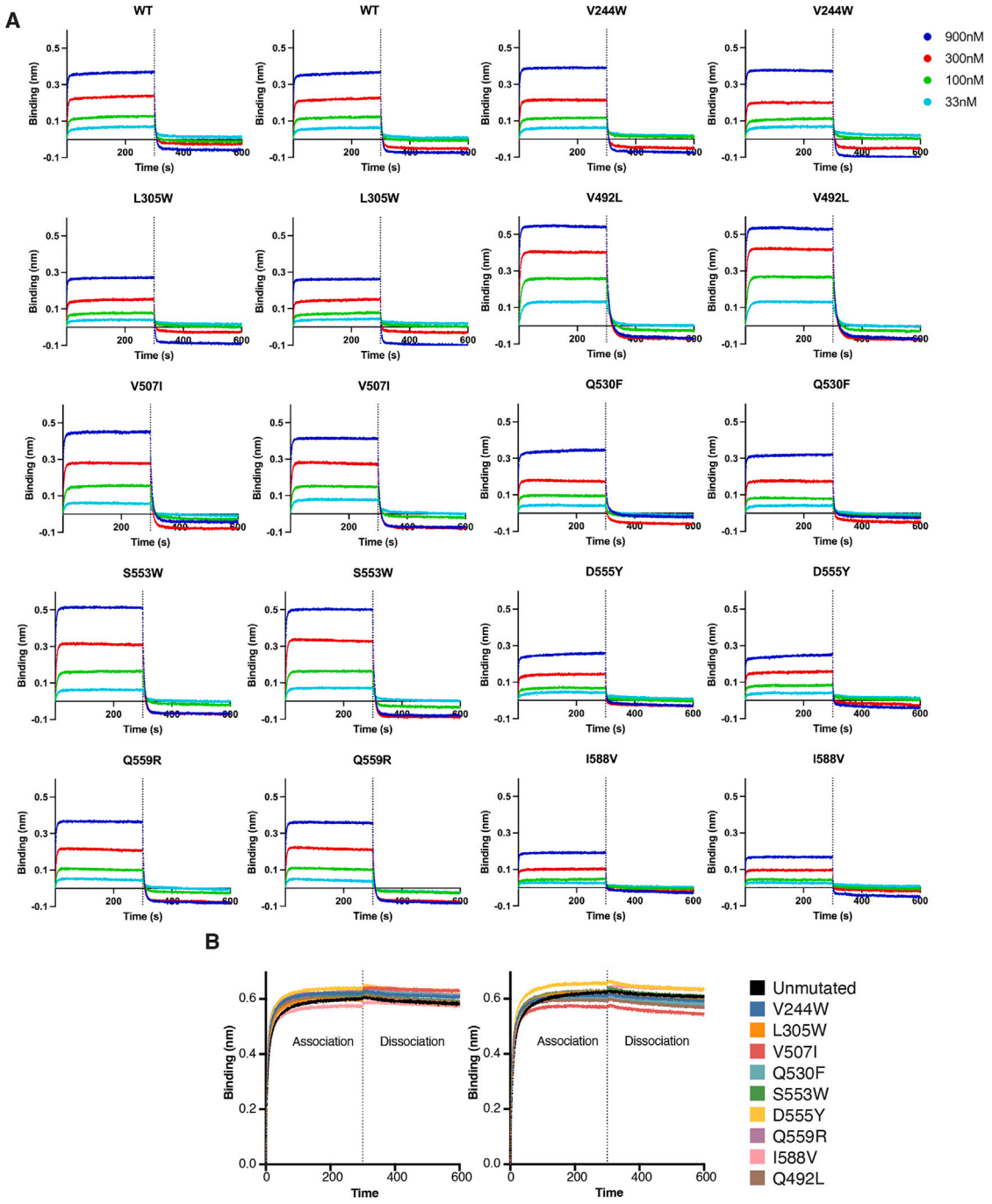

Figure S4. Biolayer interferometry binding of RBP heads to bEFNB3 or IgG, related to Figure 5

(A) BLI binding of RBP heads to bEFNB3-hFc. Data from two biological replicates (corresponding to independent batches of proteins) for binding of the monomeric RBP heads at four different concentrations to dimeric bEFNB3-hFc immobilized on AHC biosensors. The magnitude of binding was assessed by quantifying the total AUC (Table S3).

(B) BLI binding analysis of purified Nipah virus RBP head mutants at 300 nM to HENV-32 IgG immobilized on AHC biosensors. Each plot corresponds to a biological replicate using independently produced batches of proteins.

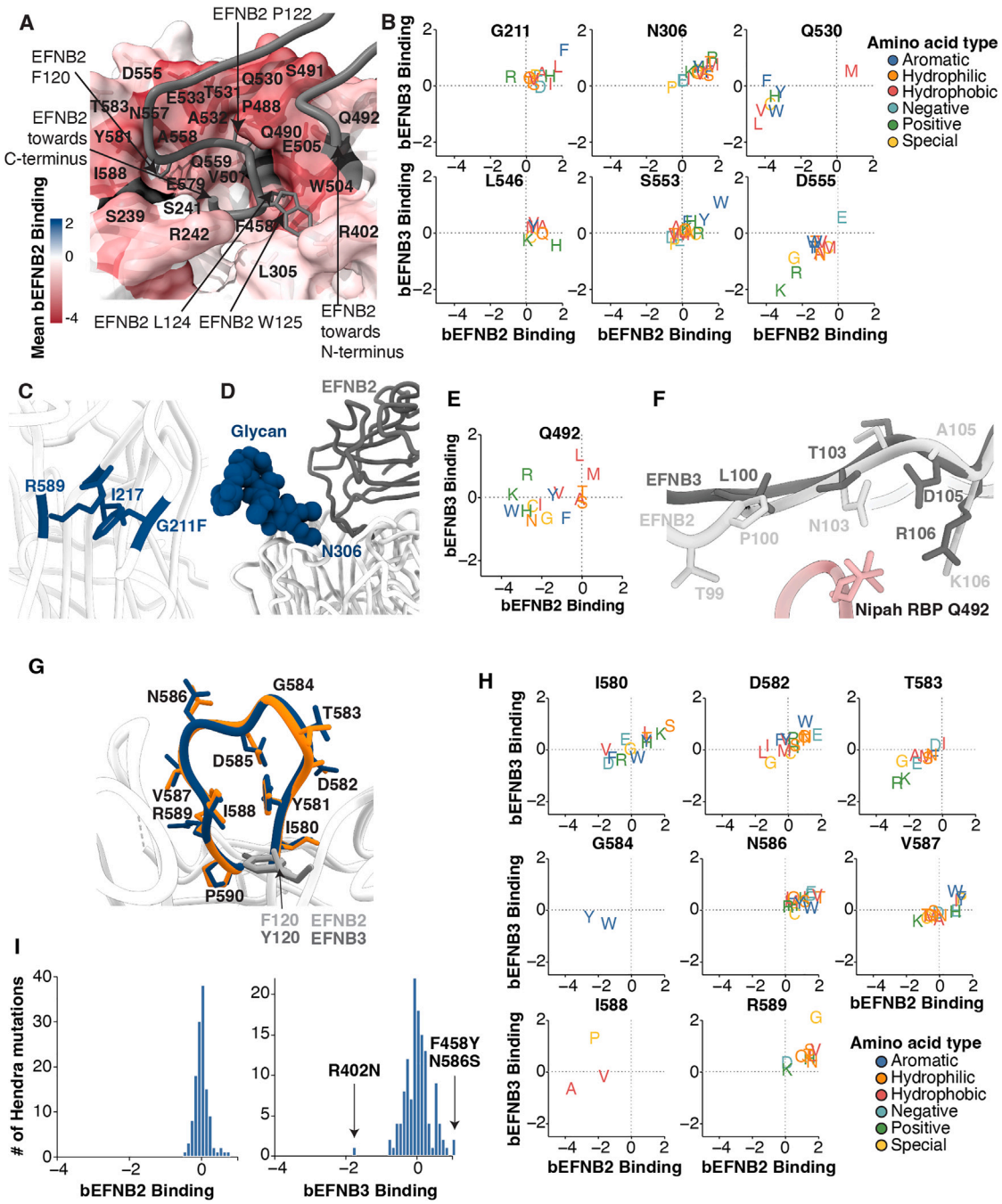

Figure S5. Additional information about effects of mutations on receptor binding, related to Figures 5 and 6

(A) Most mutations in the receptor-binding interface greatly decrease binding affinity. Average effects on bEFNB2 binding of RBP mutations at each site are mapped onto the structure of RBP bound to EFNB2 (PDB: 2VSM). A portion of the EFNB2 chain is shown (sites 100–123) in dark gray. The four amino-acid residues that insert into hydrophobic pockets on RBP's surface are shown with their side chains (ephrin sites 120, 122, 124, and 125). RBP residues colored black do not have any mutations with binding information and were filtered out due to low entry scores.

(B) Correlations between effects of mutations on binding to bEFNB2 or bEFNB3 at key sites. Each panel represents a different site, with the x axis indicating the binding to bEFNB2 and the y axis indicating the binding to bEFNB3 as measured in the DMS. The letters indicate the effects of different mutations, and the binding score for the unmutated Malaysia RBP is 0 by definition. Sites of interest highlighted in Figure 5F are shown here. Mutations of interest at these sites have large effects on binding to one or both host receptors. Briefly, G211F increases binding to both bEFNB2 and bEFNB3. Most mutations at site N306 increase binding to bEFNB2/3, likely due to the removal of a glycosylation that possibly reduces receptor binding via steric hindrance when present. Q530F greatly decreases bEFNB2 binding while maintaining bEFNB3 binding (also tested by BLI [Figure 5C] and pseudovirus neutralization (Figure 5D). L546H increases bEFNB2 binding while decreasing bEFNB3 binding. S553W/Y increases binding to both bEFNB2/3 (S553W tested by BLI (Figure 5C) and pseudovirus neutralization (Figure 5D).

(legend continued on next page)

Finally, substitutions of D555 to positively charged amino acids (K/R) greatly decrease binding to both bEFNB2/3 (D555K tested by pseudovirus neutralization; Figure 5D). An interactive plot for all sites is available at (https://dms-vep.org/Nipah_Malaysia_RBP_DMS/htmls/binding_letter_plot_slider.html).

(C) G211F increases binding to both bEFNB2 and bEFNB3 and likely increases rigidity of 203–213 loop through putative pi-cation interactions with R589 and van der Waals interactions with I217 (PDB ID: 3D11). To determine the potential orientation of the phenylalanine side chain, the most likely rotamer was selected in ChimeraX using the Dunbrack rotamer library.[73]

(D) Structural view of the glycan attached to N306 relative to the receptor. The glycan is rendered as blue spheres. PDB ID: 2VSM.

(E and F) Mutations at RBP site 492 have different effects on binding to bEFNB2 and bEFNB3 and are located near amino acids that are different between each receptor. (F) Superimposed structures of RBP bound to human EFNB2 (light gray; PDB: 2VSM) and EFNB3 (dark gray; PDB: 3D12) are shown. Receptor sites that differ between human EFNB2 and EFNB3 are labeled. Site 106 is different between bat and human EFNB2 (human to bat EFNB2 K106R, which changes it to the same residue as the one present in EFNB3). (E) Correlation between the effects of mutations on binding to bEFNB2 and bEFNB3 at site 492. Mutations to hydrophobic residues such as L and M increase binding to bEFNB3 while maintaining binding to bEFNB2. Mutations to positively charged residues (K and R) greatly decrease binding to bEFNB2 while maintaining or even increasing binding to bEFNB3. The increased binding of Q492R/K mutations is likely from a salt bridge formed with D105 in bEFNB3. Q492L affinity was directly measured by BLI (Figure 5C). Q492R was tested by pseudovirus neutralization (Figure 5D).

(G and H) Effects of mutations on binding to either bEFNB2 or bEFNB3 at RBP sites 580–590. Certain sites in the RBP loop 580–590 have mutations with large effects on binding to bEFNB2 or bEFNB3. (G) Structures of RBPs bound to either EFNB2 (colored blue; PDB: 2VSM) or EFNB3 (colored orange; PDB: 3D12). Ephrin site 120, which is an F in EFNB2 and a Y in EFNB3, is shown with distinct shades of gray. (H) Differences in effects of individual mutations on binding to either bEFNB2 or bEFNB3 at sites within the 580–590 loop. Only sites with mutations that affect binding are shown. Sites with mutations that increase binding to both bEFNB2 and bEFNB3 have side chains pointed away from the receptor-contact residue F/Y120 (sites 580, 582, 586, 587, and 589).

(I) Effects of mutations that separate Nipah and Hendra RBP on binding to bEFNB2 (left) and bEFNB3 (right) as measured in the Nipah RBP DMS. Most Hendra mutations do not affect binding to bEFNB2. For bEFNB3, one mutation (R402N) is predicted to decrease bEFNB3 binding, while two mutations (F458Y and N586S) are predicted to increase bEFNB3 binding.

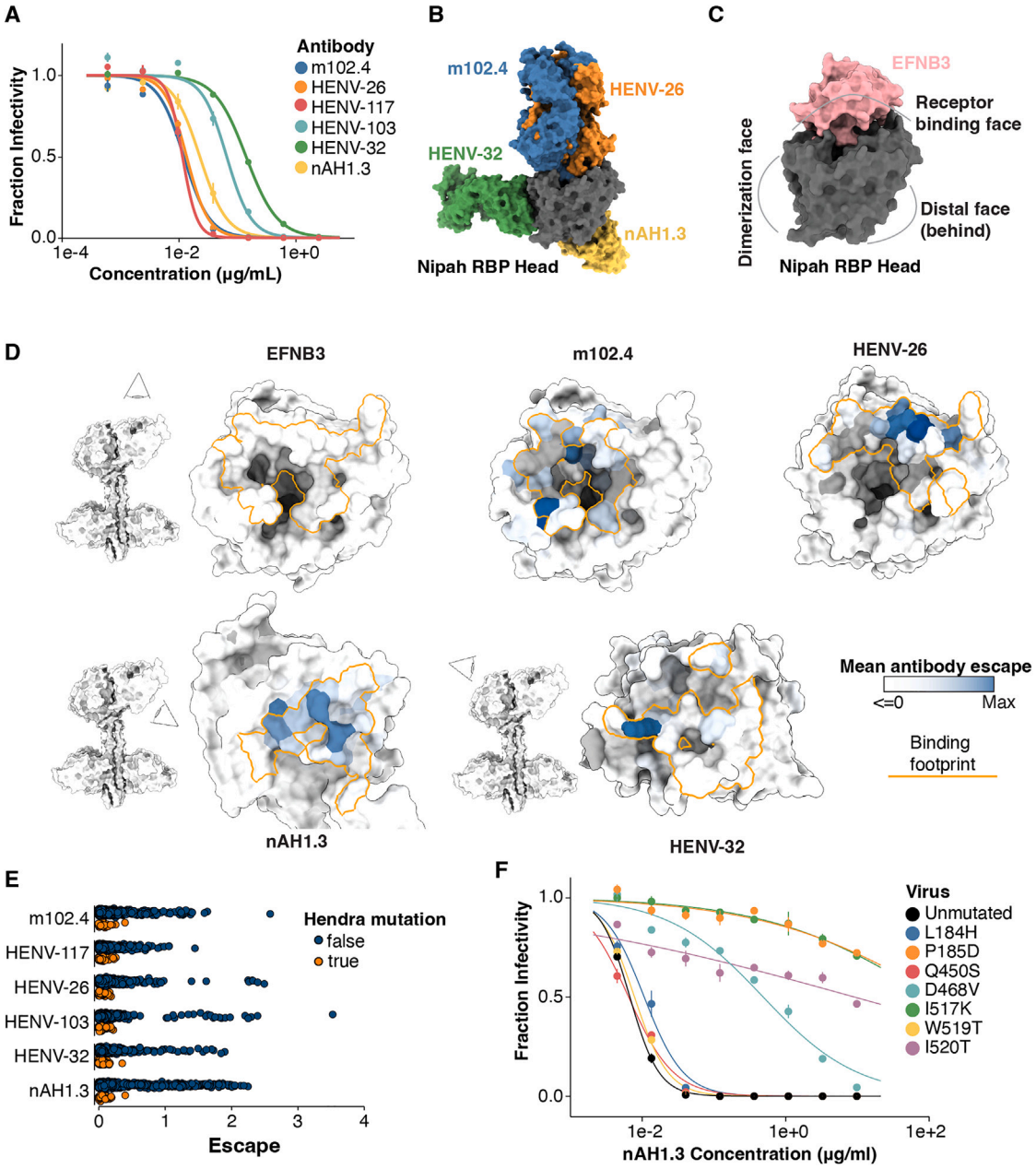

Figure S6. Additional information about antibody escape mutations, related to Figure 7

(A) Neutralization curves of unmutated pseudovirus with each antibody. Fraction infectivity was determined by incubating pseudovirus containing a luciferase reporter with eight different concentrations of antibody. 48 h after infection, luciferase signal was determined on a plate reader, and fraction infectivity was calculated by normalizing to conditions without antibody. All measurements were done in duplicate. The IC_{50} values are in Table S5.

(B) Surface rendering of antibody binding to the RBP head domain for the four antibodies with structural data.

(C) Location of epitopes on the RBP head with respect to EFNB3. RBP's head is shown in the same orientation as (B). The PDB ID for m102.4 is 6CMG, HENV-26 6VY5, HENV-32 6VY4, EFNB3 3D12, and nAH1.3 is 7TXZ. Note: for 6CMG, the structure was solved with Hendra RBP and m102.3, which is nearly identical to m102.4. For HENV-32, the structure was solved with Hendra RBP.

(D) Sites of escape are located in the antibody-binding footprints. Structures of RBP's head bound by each antibody for the four antibodies with structures available. Orange lines outline where an antibody binds, calculated as all RBP sites within 4 Å of an antibody residue. Site-average escape as measured in DMS is colored with a white-to-blue color scale (blue = higher escape), with key RBP site numbers indicated in text. Sites with no mutant data (filtered out due to having low entry) are colored light gray. The relative view of each RBP is shown with an associated eye logo and RBP tetramer. The EFNB3 binding area is shown for reference. The same PDB IDs are used from (B).

(E) Effects of Hendra mutations on antibody neutralization relative to Nipah Malaysia RBP. Hendra virus RBP mutations did not cause appreciable escape for the six monoclonal antibodies tested here when introduced individually in the Nipah virus RBP. Available Hendra virus sequences were obtained from GenBank on

(legend continued on next page)

11/17/24. All Hendra virus amino-acid mutations relative to the parental Nipah Malaysia reference strain are colored orange, while mutations not observed in Hendra virus sequences are colored blue.

(F) Neutralization curves of unmutated and single-mutant pseudoviruses against the antibody nAH1.3 to validate measurements of antibody escape from DMS. Eight different concentrations of antibody were used, and fraction infectivity was determined by comparing the luciferase signal at each concentration to the signal in the absence of antibody. Assays were performed in duplicate. The IC_{50} values from these neutralizations were used to make the correlation in Figure 7D.

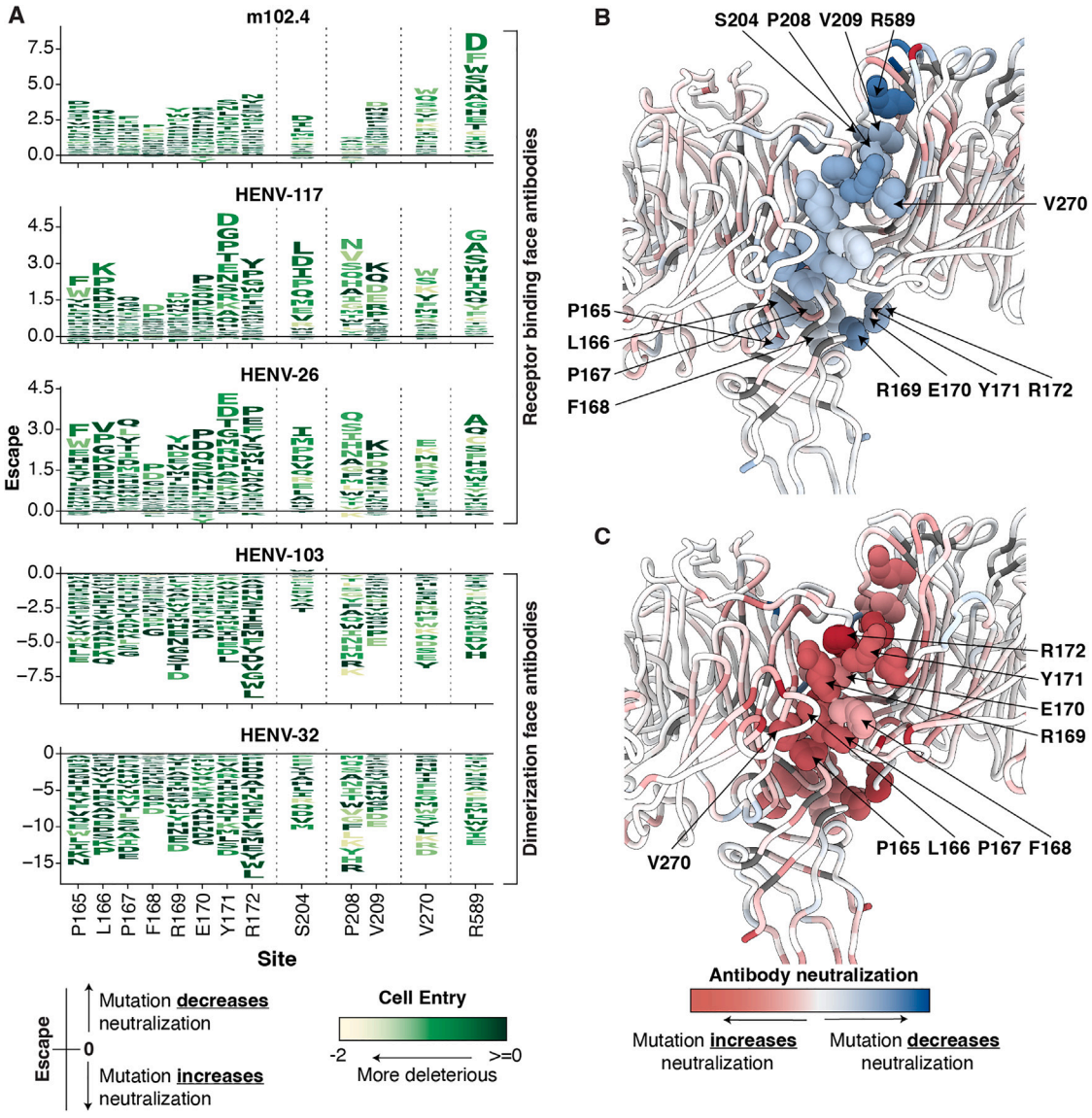

Figure S7. Opposing effects of mutations on neutralization between receptor-binding and dimerization-face-targeting antibodies, related to Figure 7

(A) Effect of mutations on antibody neutralization at specific sites. The same scale and coloring scheme is used in Figure 7A, except mutations that also increase neutralization are shown (negative letters below the center line). The height of each letter is proportional to the change in neutralization compared with the unmutated sequence. Mutations with negative scores increase neutralization by that antibody, while mutations with positive scores decrease neutralization. Note that there are escape mutations for HENV-103 and HENV-32 (Figure 7A), and they just do not fall in the 13 sites shown here.

(B and C) Averages of mutational effects on neutralization between the three receptor-binding face antibodies (B) and the two dimerization face antibodies (C) are shown. Sites with mutations that tend to increase antibody neutralization are colored red, and those that decrease neutralization are colored blue. For visual clarity, only sites in view are labeled. Sites of interest in the asymmetric distal heads are labeled once per chain. Sites in the distal head pointing up are labeled in (B), while sites in the distal head pointing down are labeled in (C). Sites with opposing effects on neutralization are located in the dimerization interface between the distal heads and likely destabilize the interaction. Dimerization-face-targeting antibodies (HENV-32 and HENV-103) likely have higher accessibility due to the destabilized interface, which increases neutralization. Conversely, destabilizing the dimer interface appears to cause moderate escape from receptor-binding face antibodies.